NEUROSCIENCE
RESEARCH ARTICLE

M. Serrano-Reyes et al. / Neuroscience 446 (2020) 304–322

Spontaneous Activity of Neuronal Ensembles in Mouse Motor Cortex: Changes after GABAergic Blockade

Miguel Serrano-Reyes, Brisa García-Vilchis, Rosa Reyes-Chapero, Verónica Alejandra Cáceres-Chávez, Dagoberto Tapia, Elvira Galarraga and José Bargas *

División de Neurociencias, Instituto de Fisiología Celular, Universidad Nacional Autónoma de México, México City 04510, Mexico

Abstract—The mouse motor cortex exhibits spontaneous activity in the form of temporal sequences of neuronal ensembles *in vitro* without the need of tissue stimulation. These neuronal ensembles are defined as groups of neurons with a strong correlation between its firing patterns, generating what appears to be a predetermined neural conduction mode that needs study. Each ensemble is commonly accompanied by one or more parvalbumin expressing neurons (PV+) or fast spiking interneurons. Many of these interneurons have functional connections between them, helping to form a circuit configuration similar to a small-world network. However, rich club metrics show that most connected neurons are neurons not expressing parvalbumin, mainly pyramidal neurons (PV−) suggesting feed-forward propagation through pyramidal cells. Ensembles with PV+ neurons are connected to these hubs. When ligand-gated fast GABAergic transmission is blocked, temporal sequences of ensembles collapse into a unique synchronous and recurrent ensemble, showing the need of inhibition for coding cortical spontaneous activity. This new ensemble has a duration and electrophysiological characteristics of brief recurrent interictal epileptiform discharges (IEDs) composed by the coactivity of both PV− and PV+ neurons, demonstrating that GABA transmission impedes its occurrence. Synchronous ensembles are clearly divided into two clusters one of them lasting longer and mainly composed by PV+ neurons. Because an ictal-like event was not recorded after several minutes of IEDs recording, it is inferred that an external stimulus and/or fast GABA transmission are necessary for its appearance, making this preparation ideal to study both the neuronal machinery to encode cortical spontaneous activity and its transformation into brief non-ictal epileptiform discharges.

Key words: motor cortex spontaneous activity, neuronal ensembles, epileptiform activity, parvalbumin expressing neurons, calcium imaging recordings, multielectrode array recordings.

INTRODUCTION

It has been postulated that neurons do not perform their functions in isolation, there is evidence that the activity of cortical circuits is generated by a network of neuronal ensembles that are activated and propagate sequentially (Hebb, 1949; Abeles, 1991; Beggs and Plenz, 2004; Ikegaya et al., 2004; Luczak et al., 2007; Pastalkova et al., 2008; Markram et al., 2015; Dechery and MacLean, 2017). Most of these studies involve sensory, motor, or decision-making tasks and have been performed both in the cortex and in other brain regions (Carrillo-Reid et al., 2008; 2016;; Buzsáki, 2010; Churchland et al., 2012; Harvey et al., 2012; Peters et al., 2014; Gründemann et al., 2019). However, there is a paucity of network analysis in non-stimulated or spontaneously active rodent motor cortex *in vitro*. We approached this study asking if the local functional architecture of the motor cortex at rest can be seen as a spontaneous temporal sequence of neuronal ensembles (Dechery and MacLean, 2017). This type of spontaneous pattern can be a model of how local activity persists through cortical circuits without stimulus (Luczak et al., 2007). In addition, we address the role of inhibitory interneurons, in particular, parvalbumin-expressing cells (PV+) or fast-spiking interneurons (FSI), during network activity, given their participation in physiological and pathological oscillations, and their special relationship with epileptogenesis (Avoli and de Curtis, 2011; Huberfeld et al., 2011; Muldoon et al., 2013, 2015; Hongo et al., 2015; Serafini et al., 2016; Smith and Schevon, 2016). We used PV-Cre mice to identify PV+ interneurons in the motor cortex. In this way, once the control properties of the rodent motor cortex were established, we proceeded to perform a pharmacological

*Corresponding author.
E-mail address: jbargas@ifc.unam.mx (J. Bargas).
Abbreviations: FSIs, fast-spiking interneurons; GABA, gamma-aminobutyric acid; IEDs, interictal epileptiform discharges; LFPs, local field potentials; MEAs, multi-electrodes arrays; PV+, parvalbumin expressing neurons; PV−, neurons not expressing parvalbumin mainly pyramidal neurons.

https://doi.org/10.1016/j.neuroscience.2020.08.025
0306-4522/

manipulation to focus the study on describing the participation of the PV+ interneurons in epileptiform events.

Epilepsy prevalence is around 65 million people worldwide (Ngugi et al., 2010). Efforts to understand the mechanisms of this disease are being done. Helpful *in vitro* models of epileptiform-like events have been developed. Some use electrical stimulation, convulsant drugs, changes in the extracellular ionic environment or combinations of these (Avoli and Jefferys, 2016). As a result, several kinds of epileptiform discharges have been described. Here, we are interested in brief and recurrent interictal epileptiform discharges (IEDs; Brückner and Heinemann, 2000; de Curtis et al., 2012), which appear between or before pre-ictal spikes or ictal-like discharges (Huberfeld et al., 2011). IEDs have been postulated to be driven by synchronized GABAergic interneurons, while pre-ictal and ictal events are thought to have a larger contribution of glutamatergic neurons (Derchansky et al., 2008; Huberfeld et al., 2011; Karlócai et al., 2014; Chang et al., 2018; Lévesque et al., 2018). However, quantitative network relationships between excitatory and inhibitory neurons during IEDs are lacking. When pre-ictal events appear, ictal events are eminent. But IEDs may not lead to full ictal discharges during long time periods, bringing the opportunity to study them in isolation, in the motor cortex, to better observe the underlying multiunit activity with single cell resolution, and separate the collective participation of GABAergic PV+ and non-GABAergic PV− (mostly glutamatergic) neuronal populations (Avoli and de Curtis, 2011; Avoli et al., 2013). GABAergic contribution to IEDs raises a question about whether they protect from or precipitate ictal events (de Curtis et al., 2012). We used a cortical *in vitro* model where GABAergic transmission is impaired by bicuculline plus Mg^{2+}-free solution (Cohen et al., 2006; de la Prida et al., 2006). It induced IED-like events in the absence of stimulation. IEDs may not lead to ictal events or seizures, although they may course with cognitive and memory disabilities (Binnie, 2003; Holmes and Lenck-Santini, 2006; Zhou et al., 2007; Mosbah et al., 2014). We use multirecording techniques such as calcium imaging and multi-electrodes arrays (MEAs) to visualize and record multiple neurons simultaneously with single cell resolution (Sasaki et al., 2007; Karlócai et al., 2014; Levesque et al., 2018; Sadovsky and MacLean, 2013), as well as targeted single cell recordings with the whole-cell technique to analyze neuronal and network dynamics during IEDs.

Pharmacological manipulations including high K^+, low Mg^{2+}, low Ca^{2+}, 4-aminopyridine, alkalinization, pilocarpine, etc. are needed to induce ictal-like events in *in vitro* slices. Simple manipulations such as bicuculline plus Mg^{2+}-free solutions may fail to induce ictal events (Huberfeld et al., 2011; Karlócai et al., 2014). Here we show that recurrent IEDs can be generated by a blockade of GABAergic transmission. They can be recorded for several minutes without inducing ictal-like events. In the last decade, similar studies have distinguished putative pyramidal neurons and FSI interneurons through the shape of their spikes in extracellular recordings (Sakata and Harris, 2009; Gonzalez-Sulser et al., 2012; Lévesque et al., 2018). Contradictory results have been obtained related to the participation of PV+ interneurons in different epileptiform phenomena, some data show that their activation prevent the spread of seizures or their duration (Cammarota et al., 2013; Krook-Magnuson et al., 2013). In contrast, optogenetic stimulation of interneurons promote ictal-like events (Sessolo et al., 2015; Khoshkhoo et al., 2017; Chang et al., 2018) implying GABAergic transmission in their generation. Here we use multi-recording techniques that allow elucidate the role of PV+ and PV− neurons in control and during IEDs. This shows a way to study other neuronal phenotypes during control, stimulated circuitry, pre-ictal and ictal phenomena.

EXPERIMENTAL PROCEDURES

Animal use and care

B6;129P2-*Pvalb*$^{tm1(cre)Arbr}$/J (JAX stock:017320, Hippenmeyer et al., 2005) mice were acquired from Jackson Laboratories (https://www.jax.org/), and mating was carried out between homozygous mice. However, female and male heterozygous mice were backcrossed every five generations with our background wild C57BL/6 NHsd mice and later bred with their littermates to obtain homozygous mice as recommended (https://www.jax.org/news-and-insights/jax-blog/2018/april/how-to-refresh-your-mutant-or-transgenic-mouse-strains#)". A total of 36 male and female animals were used for all experimental groups. *In vitro* experiments were performed on PV-Cre knockin mice of both sexes at postnatal days (PD) 40–50. We accomplish the international guidelines for the ethical use of experimental animals established in the National Institutes of Health Guide for Care and Use of Laboratory Animals Eighth Edition (NIH, 2010). The detailed protocols were approved by the Institutional Committee for Laboratory Animals Care of the Instituto de Fisiología Celular (IFC), UNAM (NOM-062-Z00-1999; laboratory protocols JBD-59-15). They were housed in a temperature-controlled, pathogen-free room, on a 12 h light–dark cycle, and allowed food and water ad libitum, minimizing the number of animals to achieve statistical significance and the avoidance of animal suffering.

Viral infection

Stereotaxic surgeries were performed at PD 21 injecting 0.5 μL of viral vectors with a dental needle in coordinates from Bregma, AP +1.5 mm, ML −1.2 mm and DV +1.2 mm to a 0.1 μL/min rate to co-express pAAV.Syn.GCaMP6f.WPRE.SV40 for expression in all neurons and AAV pCAG-FLEX-tdTomato-WPRE into PV+ neurons (Chen et al., 2013; Oh et al., 2014). Co-expression dilutions were always 1:1 for calcium imaging recordings (n = 13 animals). To perform surgeries, animals were anesthetized by intraperitoneal injection of ketamine/xylazine (85/15 mg/kg) solution. Several measures were taken to minimize pain and discomfort. For stereotaxic surgery artificial tears were placed in the mice's eyes to avoid damage. Body temperature was modulated with a heating pad peri- and post-operatively until animal full recovery. During this period mice received

chocolate pellets ad libitum and subcutaneous 100 μL glucose 2% in saline solution daily injections were administered if more than 20% weight loss was detected. 80% of injected mice survived.

Slice preparation

Mice were anesthetized intraperitoneally with ketamine/xylazine (85/15 mg/kg) and perfused with an iced saline solution containing (in mM): 2.5 KCl, 28 $NaHCO_3$, 0.4 $CaCl_2$, 7 $MgCl_2$, 1.44 NaH_2PO_4, 7 dextrose, 4.5 pyruvate, 0.28 ascorbic acid and 234 sucrose (300 mOsm/l, pH 7.4) gassed with 95% O_2 and 5% CO_2 in order to remove their brains while preserving cellular viability. Parasagittal brain slices were obtained (250 μm thick) using a vibratome (Pelco, Ted Pella, Redding, CA, USA). Afterwards, slices were transferred to saline containing (in mM): 126 NaCl, 3.5 KCl, 26 $NaHCO_3$, 1.5 $CaCl_2$, 1 $MgCl_2$, 1.2 NaH_2PO_4, 15 dextrose, 0.2 thiourea and 0.2 ascorbic acid (300 mOsm/l, pH 7.4) at room temperature for at least 1 h before performing *in vitro* experiments. During all treatments, the saline containing the slices were continuously gassed with 95% O_2 and 5% CO_2 set at 32 °C (TC02, Multichannel systems, SE. Harvard Bioscience, Inc.).

Patch-clamp recordings

Whole-cell patch-clamp recordings were performed from pyramidal neurons and PV+ interneurons labeled with td-Tomato in layer 5 of motor cortex using micropipettes made with borosilicate glass (3–6 MΩ) filled with (in mM): 120 $KMeSO_4$, 2 $MgCl_2$, 10 HEPES, 10 EGTA, 1 $CaCl_2$, 0,2 Na_2ATP, 0,2 Na_3GTP and 1% biocytin. Responses were acquired with an Axoclamp 2B amplifier (Axon Instruments, Foster City, CA, USA). The signals were digitized at 10 kHz using an AT-MIO-16E4 board (National Instruments, Austin, TX, USA) and saved in a PC computer using Im-Patch© (http://impatch.ifc.unam.mx/). Neurons whose access resistance changed >20% during recordings were discarded. The plateau duration of bursts was calculated by measuring the time elapsed from the first to the last spike (Arias-García et al., 2018).

Immunohistochemistry

Following patch-clamp recordings, the slices were fixed in 4% paraformaldehyde and 1% saturated picric acid in 0.1 M phosphate buffer (PB; pH = 7.4) at 4 °C. Biocytin-filled cells were visualized by incubating slices in 1:200 streptavidin-Cy3 or FITC conjugate (Invitrogen) in PBS containing 0.3% Triton X-100 (PBS-Tx) overnight at 4 °C. To perform immunohistochemistry to visualize PV + neurons the brains were removed and post-fixed for 24 h in 4% paraformaldehyde in PBS, before being cryopreserved in 30% sucrose at 4 °C. The brains were then cut on a vibratome into 40 μm slices. Free-floating slices were first incubated 30 min with 1% bovine albumina to block nonspecific binding sites and for 24 h with a rabbit PV antibody against parvalbumin (anti PV 1:2000 Abcam) dissolved in PBS containing 0.25% Triton-X. The slices were then rinsed three times with PBS and incubated with a goat versus rabbit secondary antibody (1:200) during 1 h. The secondary antibodies used for immunofluorescence included fluorescein (FITC)-conjugated anti-rabbit IgG (Vector Laboratories, Burlingame, California, USA) for detecting the anti- PV antibody (Ibanez-Sandoval et al., 2006). All sections were mounted in Vectashield medium (Vector Laboratories). Images were acquired with an LSM700 Zeiss confocal laser scanning microscope (Zeiss, Gottingen, Germany). Single section confocal images (1024 × 1024) were collected and exported to TIFF file format (Ibanez-Sandoval et al., 2016).

Calcium imaging recordings

Imaging of spontaneous Ca^{2+} signals in deep layers of non-stimulated motor cortex were performed. Image sequences (movies) at six frames per second were captured with a microscope (XLUMPlanFI, Olympus, Center Valley, PA, USA) equipped with a 10×, 0.3 NA water-immersion objective. A Lambda LS illuminator (Sutter instruments, Petaluma, CA) coupled to specific excitation-emission filters (GCamp6f; excitation: band-pass 470–40 nm, emission: band-pass 520–40 nm and td-Tomato; excitation: band-pass 535/50 nm, emission: high-pass 590 nm) and a CoolSnap K4 camera, controlled by Im-Patch© software were used. Spontaneous activity was recorded for 10 min, thereafter, 10 μM bicuculline (Sigma-Aldrich 14,343 – 50 MG) were added under Mg^{2+}-free conditions. Once installed, IEDs were recorded for another 10 min and compared with control conditions, however, longer recordings could be done. Transition from control activity to IEDs generation is the subject of another work. Previous to the experiment, a digital camera picture was taken with the specific filter to identify the neurons labeled with td-Tomato.

Image analysis

Image processing was performed with custom-written plugins in ImageJ (1.51j8, National Institutes of Health). Coordinates of the regions of interest (ROIs; neurons containing GCaMP6f) were manually identified with a circular template whose radius was chosen in each case. For each ROI, the change in somatic fluorescence (ΔF/F) was calculated as $(F_1 - F_0)/F_0$ in each frame, where F_1 is the fluorescence intensity at any time point, and F_0 is the local background fluorescence intensity of the ROI (four times the ROI diameter).

Detection of neuronal activity from calcium imaging

All analyses were performed with custom-written programs in MATLAB (2019a, MathWorks, Natick, MA, USA). All recordings were examined manually to remove artifacts. Calcium signals of the ROIs were deconvolved into trains of inferred action potentials with a modified version of the fast-oopsi algorithm (Vogelstein et al., 2010). Threshold to detect spike probability was two standard deviations (SD) for each neuron,

the values above were set to 1, and the values below were set to 0. Once this was done, a [$N \times F$] binary matrix (raster matrix) was built, where N denotes the number of neurons (y-axis) and F represents the number of frames (x-axis transformed to time in minutes or seconds). Each row in the raster matrix represents the activity of one neuron.

Extracellular multi-electrode array (MEA) recordings

The experimental protocol was conducted in the same way as in calcium imaging experiments. Extracellular recordings were performed using the MEA2100-System (Multichannel systems). Slices were positioned in the chamber of a perforated microelectrode array. The array is a 12×12 titanium nitride electrode grid, of 30 μm diameter, 200 μm inter-electrode distance and < 100 kΩ impedance (120pMEA200/30iR-Ti, Multichannel systems). The upper and lower solution inflow was 6 ml/min using a peristaltic perfusion system (PPS2, Multichannel systems). Raw data was digitized at 25 kHz. At the end of the experiment, a digital camera picture of the slice position was taken.

Detection of neuronal activity in extracellular MEA recordings

All analyses were performed with custom-written programs in MATLAB and MultiChannel Analyzer software (2.8.2.18079, multichannel systems). The raw signal of each electrode was processed with a bandpass filter (500–5000 Hz). Events that exceeded six times the SD of the baseline signal were identified as action potentials and individual units recorded in each electrode were distinguished by grouping spikes with similar shapes (amplitude, width and after-potential). To achieve this, the correlation coefficient between all the spikes of a given electrode was calculated, this information was used to build a network where each node corresponds to a spike and the connection between them represents its correlation between pairs. With this network, a community detection was performed that automatically revealed the units of each electrode because spikes with the same shapes ended up grouping together (Newman, 2006). Detected spikes were converted to binary times of occurrence with a 1-ms bin. These binary times of individual units were used to build an [$N \times F$] raster matrix (as in calcium imaging). The local field potential (LFP) signal was acquired with a low-pass filter (100 Hz) applied to the raw signal. The LFP spectrogram was estimated using interval sizes set to sampling frequency. The sampling frequency was also used to fix the number of points to use in the Fourier transform; the overlap between intervals was set to 95%.

Detection of neuronal ensembles

All analyses were performed with custom-written programs in MATLAB. In order to identify neuronal ensembles in a raster matrix, a [$N \times N$] pair to pair correlation matrix was obtained between the row values of the raster matrix (Pearson's correlation coefficient between all neuron pairs). The correlation matrix was used as an adjacent matrix to build a binary functional network in which neurons are the nodes and significant correlation values were maintained as links. Monte Carlo simulations with 10,000 surrogate raster matrixes that shuffle the activity time of the original neurons while maintaining their inter-spike intervals (Bruno et al., 2015; Pérez-Ortega et al., 2016) were used to obtain significant probability values. In addition, due to the significant spontaneous activity of cortical tissue, the adjacent matrix built by detecting groups of neurons with correlated activity was tuned up by detecting communities in a network using the modularity algorithm (Newman 2006) under an assumption-free analyses of spatiotemporal firing patterns. The advantage of this grouping method is that there is no need to use a rule or stimulus to propose a number of groups in the network: strongly linked neuronal communities were detected by maximizing the parameter $Q = \{\text{number of links within a module}\} - \{\text{expected number of such links}\}$ making an algorithm to perform a number of iterations that automatically reveal the optimal number of groups (see Supplementary movie V1). Strongly correlated groups with different activity patterns between communities are here referred to as neuronal ensembles (Lampl et al., 1999; Luczak et al., 2007). Nearly coactive neurons at each time interval were obtained by adding the columns of the raster matrices. The sum was done in 5 ms intervals except in the experiments with calcium imaging where the raw sum of the matrix column was made (each frame lasts 1/6 seconds). Each IED was identified as an event larger than 5 SDs from the coactivity signal, the maximum value was considered as time zero of the IED. Half-width of the IEDs was calculated as the duration of coactive events at half the maximum amplitude.

Network analysis

The experimentally obtained neural networks can be described using Graph Theory, this approach is useful to describe and predict the structural and dynamic behavior of networks (Feldt et al., 2011; Fornito et al., 2016). Characteristic measures of network organization were computed: (1) ratio edges/nodes, to compare the density of connections, (2) Degree (k), the number of links that connect a node to other elements of the network. (3) Characteristic path length (L), the average path length among all possible node pairs in a network. A path is understood as an ordered sequence of edges in a graph. (4) Clustering coefficient (C), a topological measure of the tendency of two nodes, connected to a third one, to also connect to each other. (5) Modularity (Q), parameter related to the subdivision of a graph into strongly interconnected groups, it is obtained by calculating the number of links that exist within the groups minus the expected number of connections in an equivalent network with randomly placed edges (Newman, 2006; Feldt et al., 2011; Cossart, 2014). In addition, the normalized degree distribution $P(k_n)$ was obtained: probability that a node has k/k_{max} connections in each experiment. The computation of network parameters was performed with the algorithms present in the Brain Connectivity Toolbox

(https://sites.google.com/site/bctnet/). Network visualization was done using the open source graph visualization platform Gephi (https://gephi.org/).

To test the tendency for high-degree neurons to be more densely functionally connected among themselves than with neurons of a lower degree, the rich-club coefficient was calculated. For a given network, the degree of each node was calculated, the nodes with the smallest degree values were incrementally removed, from the network that remains in each step. The rich-club coefficient was calculated as the ratio of connections present between the still existing nodes and the total number of possible connections that would be present when the graph would be entirely connected. The rich-club coefficient is typically normalized regarding to an equivalent random network of equal size and similar connectivity distribution. A normalized coefficient with values >1 in a growing range of k reveals the existence of a rich club organization in the network (Colizza et al., 2006; van den Heuvel and Sporns, 2011).

To make sure whether our neural networks had "small world" properties (that is, high grouping but with short path lengths between its nodes), we use a quantitative measure called small-world-ness of a network. This metric is $S_w = (L/L_R) - (C/C_L)$, where C_L is the C from the corresponding regular lattice and L_R is the L from the random graph (both from the Watts-Strogatz model with $P = 0$ and $P = 1$). When this metric is close to 1, the network behaves like a random network. Whereas, when it is close to -1 is more a regular lattice network. When the value is about 0 the network shows a stronger small-world-ness feature (Watts and Strogatz, 1998; Boccaletti et al., 2006; Pérez-Ortega et al., 2016; She et al., 2016).

Statistical analysis

Differences between multiple groups were analyzed for statistical significance with Kruskal–Wallis ANOVA tests. Parameters distributions between the different samples were compared with the Kolmogorov–Smirnov test and Wilcoxon's signed-rank test was used for paired groups. Unless indicated otherwise, all data are presented as means ± 2 standard errors of the mean (SEMs). In all analyses, $P < 0.05$ was taken to indicate statistical significance.

RESULTS

Functional architecture of spontaneous dynamics in control mouse motor cortex

To observe the network dynamics of spontaneous neuronal activity in mice motor cortex we used mouse parasagittal slices maintained *in vitro* (see box in Fig. 1A) and focused our interest in layers 5 and 6 for the acquisition of calcium imaging videos of multiple neurons with single cell resolution. This region was also used to acquire electrophysiological recordings of targeted cells. In order to validate that the fluorescence changes obtained in the experiments correspond to action potentials firing simultaneous current-clamp and calcium imaging recordings in whole-cell configuration was performed. Fig. 1B shows intracellular labeling with biocytin. Voltage responses of the same neuron evoked with depolarizing and hyperpolarizing intracellular current injections (Fig. 1C) are also shown. Fig. 1D shows simultaneous recordings of trains of action potentials evoked with depolarizing current injections (not shown) of increasing intensities illustrated at different time bases in the first and second rows. Third row shows intracellular calcium transients generated by the firing of action potentials from the same recorded neuron. From these calcium signals, the probability of action potentials firing was obtained using the fast-oopsi algorithm (Vogelstein et al., 2010) and illustrated in the fourth row. Inferred action potentials are then shown in the fifth row with a threshold of 2 SD. Inferred spikes closely follow real evoked ones as seen by comparing the second and fifth rows. Inferred spikes were used in raster plots of several neurons obtained with calcium imaging (Theis et al., 2016).

After calcium imaging of several neurons, raster plots of their spontaneous activity along time were built (Fig. 2A), where each row denotes activity of one neuron (*y*-axis). Our grouping method (paired cell to cell correlations with modularity optimization; see Experimental procedures and Supplementary movie V1 for a graphic demonstration) allowed sorting the neurons into groups with similar firing patterns, here called neuronal ensembles represented with different colors (Hebb, 1949; Abeles, 1991; Beggs and Plenz, 2004; Ikegaya et al., 2004; Markram et al., 2015; Dechery and MacLean, 2017; Buzsáki and Tingley, 2018). Here we show that the spontaneous activity of cortical networks at rest (without stimulation) consists in temporal sequences of these ensembles. To observe control spontaneous firing before using a grouping method see Supplementary Fig. S1. Ensembles emerge spontaneously and fade away as in *in vivo* experiments during task performance (Pastalkova et al., 2008). A coactivity histogram of the raster plot (black trace at the bottom in Fig. 2A), shows the typical noisy population activity of cortical resting tissue-without stimulation (Markram et al., 2015). However, underlying this population activity, similar plots taken from different neuronal ensembles clearly show a temporal sequence (denoted by different colors; Luczak et al., 2007). This behavior was stable and recurrent during several minutes. A graph preserving the original coordinates in the tissue is illustrated in Fig. 2B: nodes are the active neurons and links represent significant correlations between their firing patterns. Colors represent identified neuronal ensembles. Node sizes denote number of links (degree). Some neurons appear more connected than others. In order to analyze experiments that share similar characteristics, Fig. 2C shows the accumulated neuronal activity of each slice considered in the study ($n = 10$ out of 10 slices from different animals; vertical bars represent 1 SD in both directions). The neural networks obtained in each experiment did not show significant differences in their degree distributions (not shown). Recorded neurons were intermingled since correlation within group distance

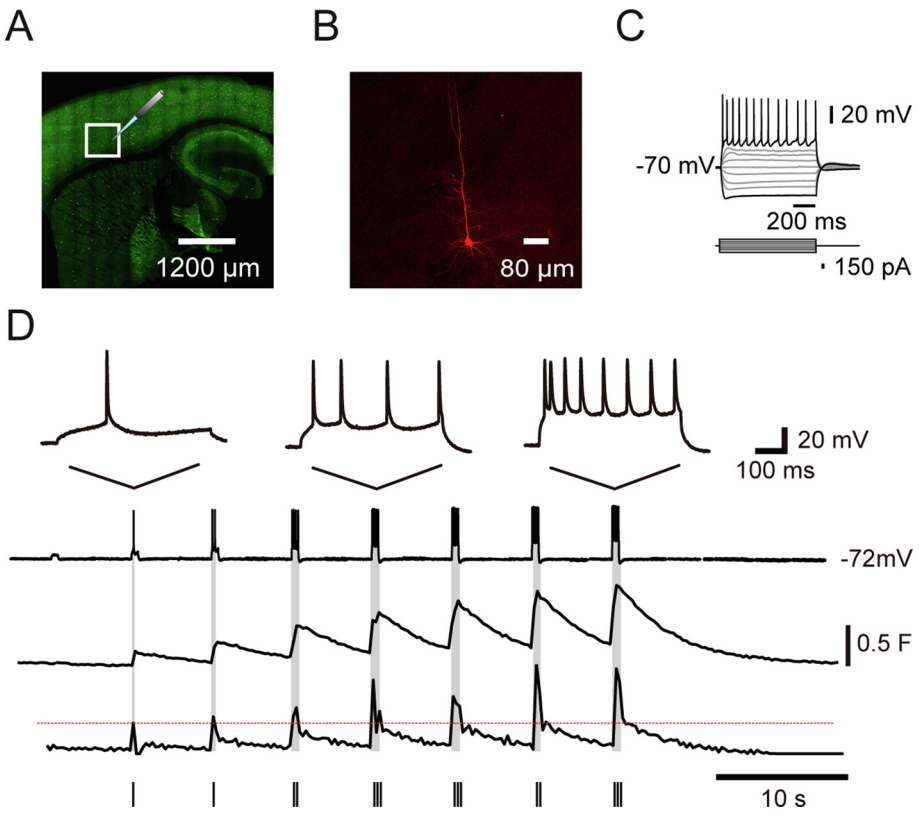

Fig. 1. Simultaneous calcium imaging and electrophysiology in a mouse motor cortex slice. **(A)** The schematic shows a photograph of a mouse parasagittal slice with PV immunoreactivity, the white box represents the calcium imaging video acquisition site and the region where electrophysiological and fluorescence recordings were made. **(B)** A recorded neuron was filled with streptavidin-Cy3 conjugated biocytin (red) showing a pyramidal phenotype. **(C)** Voltage responses (top) of the neuron evoked with depolarizing and hyperpolarizing intracellular current injections of different magnitudes (bottom). The cell exhibited regular spiking, the typical response pattern of a pyramidal neuron. **(D)** Simultaneous electrophysiological recordings of action potentials (first and second rows) and intracellular calcium transients generated by electrical activity (third row) evoked with intracellular current injections of increasing intensity (not shown; first row amplifies some events of the second row) in the same neuron. From calcium signals the probability of action potentials firing was inferred (fourth row) with the fast-oopsi algorithm, the probability of inferred spikes (fifth row) has a threshold of 2 SD (red dotted line) of the total signal. Inferred spikes closely followed evoked ones (cf., second and fifth row). (For interpretation of the references to colour in this figure legend, the reader is referred to the web version of this article.)

and across groups distance was significant (Fig. 2D; $R^2 = 0.67$; $P < 0.001$; similar in seven slices examined; $P < 0.001$. One slice only had $P = 0.014$, slices were taken from different animals). Fig. 2E illustrates the distributions of normalized and significant functional connections between neurons both in a single experiment ($n = 71$ neurons, light gray) and in all experiments ($n = 427$ neurons, dark gray; 8.9 ± 1.2 neurons per ensemble; $n = 48$ ensembles from ten animals). Note descending distributions: nodes with higher degree appear with less probability. Finally, a sorted circular representation of the microcircuit (Fig. 2F) shows interactions between neuronal ensembles during spontaneous activity.

Participation of PV+ interneurons within neuronal ensembles

One acquisition field of a calcium imaging video showing the location of neurons labeled with td-Tomato (PV+) marked with red arrows (Fig. 3A). Panels in Fig. 3B are different frames of an image sequence showing that different neurons expressing GCaMP6f are active at different moments, among them, PV+ interneurons (red arrows) previously identified with td-Tomato. A representative raster plot of the spontaneous activity in motor cortex taken from a slice and animal different to the ones shown in Fig. 2 is illustrated (Fig. 3C top). A temporal sequence of neuronal ensembles is shown using different colors. In addition, the activity of PV+ interneurons is indicated with darker colors and by the arrowheads on the right. Interestingly, almost each neuronal ensemble had the accompanying firing of a PV+ interneuron (80.2 ± 0.1% of the ensembles; $n = 10$ slices from different animals), a result highly improbable to happen at random (25.5 ± 6%; $P < 0.001$; comparing 10,000 surrogate raster plots for each of $n = 10$ slices from ten different animals). The participation of PV+ neurons in network activity is sparse as compared to PV− neurons. At the bottom, the global coactivity histogram (black) shows the noisy population activity of the resting cortex. However, coactivity obtained for the different ensembles (colored) shows that behind this apparent chaotic behavior there is an ordered sequence of neuronal ensembles that go on and off with a certain level of intersection. A circular visualization of this microcircuit shows the location of PV+ interneurons within ensembles (Fig. 3D arrow heads). Even if most significant functional connections are within ensembles, including those of PV+ interneurons, some connections cross to other ensembles, and some of these crossings belong to interneurons. Distribution of the number of normalized connections of PV+ neurons (dark gray, $n = 70$ neurons from 10 animals) and PV− neurons (light gray, $n = 357$ neurons from ten animals) have a similar shape, in both cases highly connected neurons have less probability (Fig. 3E). The distribution has an elongated tail, revealing the existence of a small number of highly interconnected neurons, known as hubs. There are several metrics (mainly node degree) that use this concept and generally converge on the idea that they correspond to topologically central nodes positioned in such a way that they have a strong influence on the

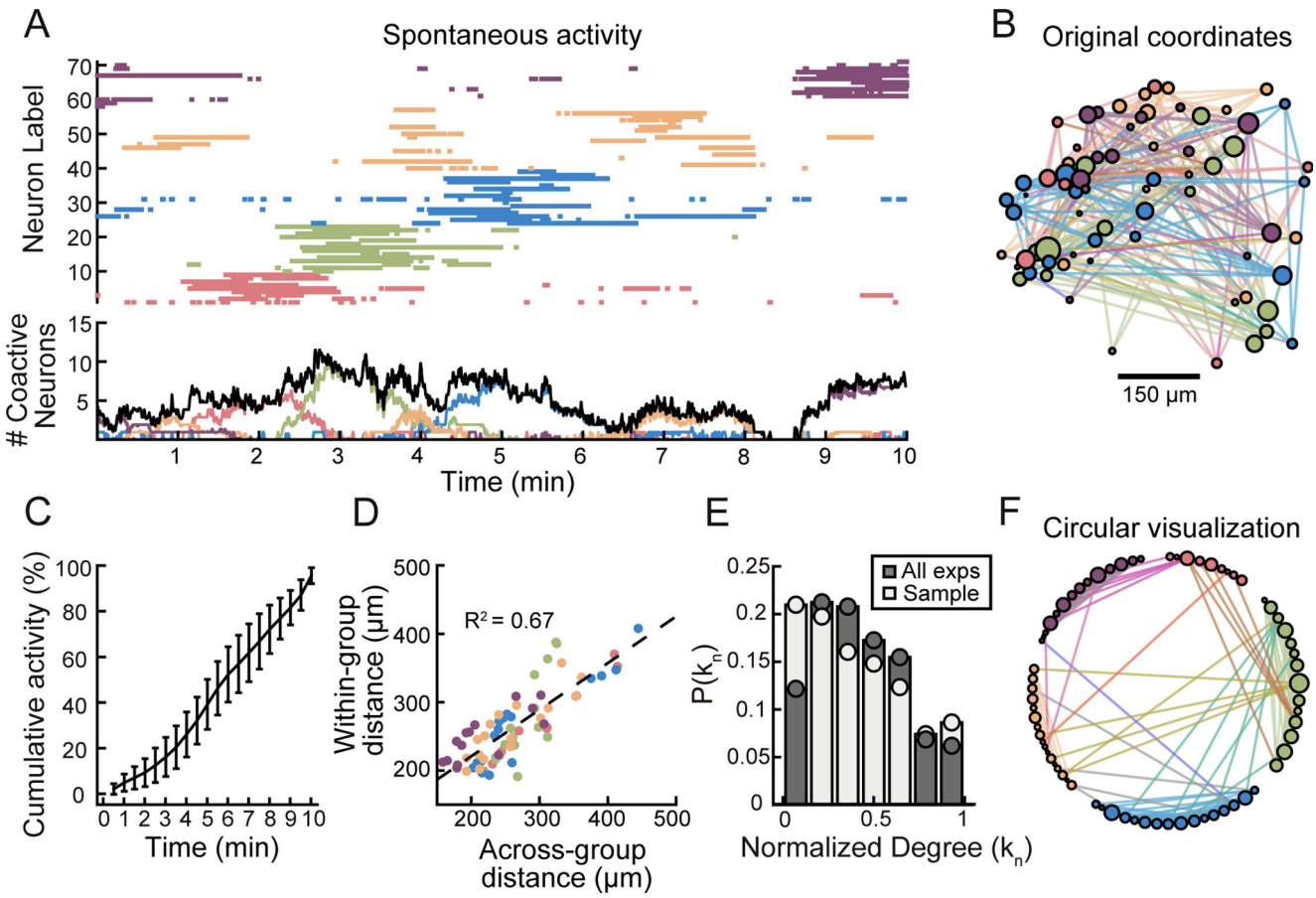

Fig. 2. Spontaneous dynamics of neuronal ensembles in control mouse motor cortex. **(A)** Raster plot of the spontaneous activity of several neurons along time in motor cortex, each row denotes activity in one neuron (*y*-axis); the color represents the belonging of each neuron to identified neuronal ensembles by means of paired cell to cell correlations (see Methods). Histogram of the summed activity of neurons in time (black trace at the bottom) plus histograms for each ensemble shown with corresponding colored traces; note the temporal sequence. **(B)** Graph of the cortical microcircuit preserving the original coordinates in the tissue, each neuron is a node and each line joining them represents the existence of significant correlation between their firing patterns throughout the experiment. Colors represent the neuronal ensembles identified in **(A)**, the size of the node represents number of connections with respect to others, there are highly connected nodes in the network (hubs) distributed among the different neuronal ensembles. **(C)** Behavior of the cumulative neuronal activity of all recorded slices (n = 10), vertical bars represent 1 SD in both directions. **(D)** Within group distance as a function of across groups distance for each neuron (R^2 = 0.67; P < 0.001), colors denote their ensemble membership as shown in A. **(E)** Distribution of normalized functional connections between neurons in a single experiment (light gray, n = 71 neurons) and in all experiments (dark gray, n = 427 neurons). **(F)** Sorted circular representation of the microcircuit network shown in **(B)**, the coordinates have been regrouped in the different neuronal ensembles to show the interactions that occurred during cortical spontaneous activity. The size of the node represents its number of connections (degree). (For interpretation of the references to colour in this figure legend, the reader is referred to the web version of this article.)

local circuitry to which they belong. It is possible to define a core based on the density of connectivity between the hubs of a given network. This is what the rich club analyses means: it finds and describes the subset of high-degree nodes that are more densely connected to each other than expected by chance (Colizza et al., 2006; Feldt et al., 2011; van den Heuvel and Sporns, 2011). The rich-club coefficient as a function of degree (k) compared against the same coefficient for a random network of equal size and similar connectivity distribution (black line vs gray line) shows a significant rich-club behavior of the neural network structure between 4 and 12 functional connections. It is shown by values greater than 1 of the normalized rich-club coefficient (red line) that increases as a function of k (Fig. 3F). Different characteristics of PV+ functional connectivity are illustrated by box plots of Fig. 3G: PV+ interneurons connecting with other PV+ interneurons are near 45 ± 14%, connections with other ensembles different to the one they belong are about 57 ± 14%, and PV+ interneurons belonging to the rich club are about 75 ± 10% (n = 10 slices from ten different animals). In the rich club network PV+ neurons are signaled with arrow heads. Note that nodes with higher degrees are not PV+ interneurons. However, all clusters with PV+ neurons connect with these highly connected PV− neurons (in blue, Fig. 3H).

Participation of PV+ interneurons during IEDs

In order to observe what happens to the control circuit when fast ligand-gated $GABA_A$-receptor mediated transmission is blocked, 10 µM bicuculline were added to a virtual Mg^{2+}-free saline solution. This is one of many ways to induce epileptiform discharges (Cohen

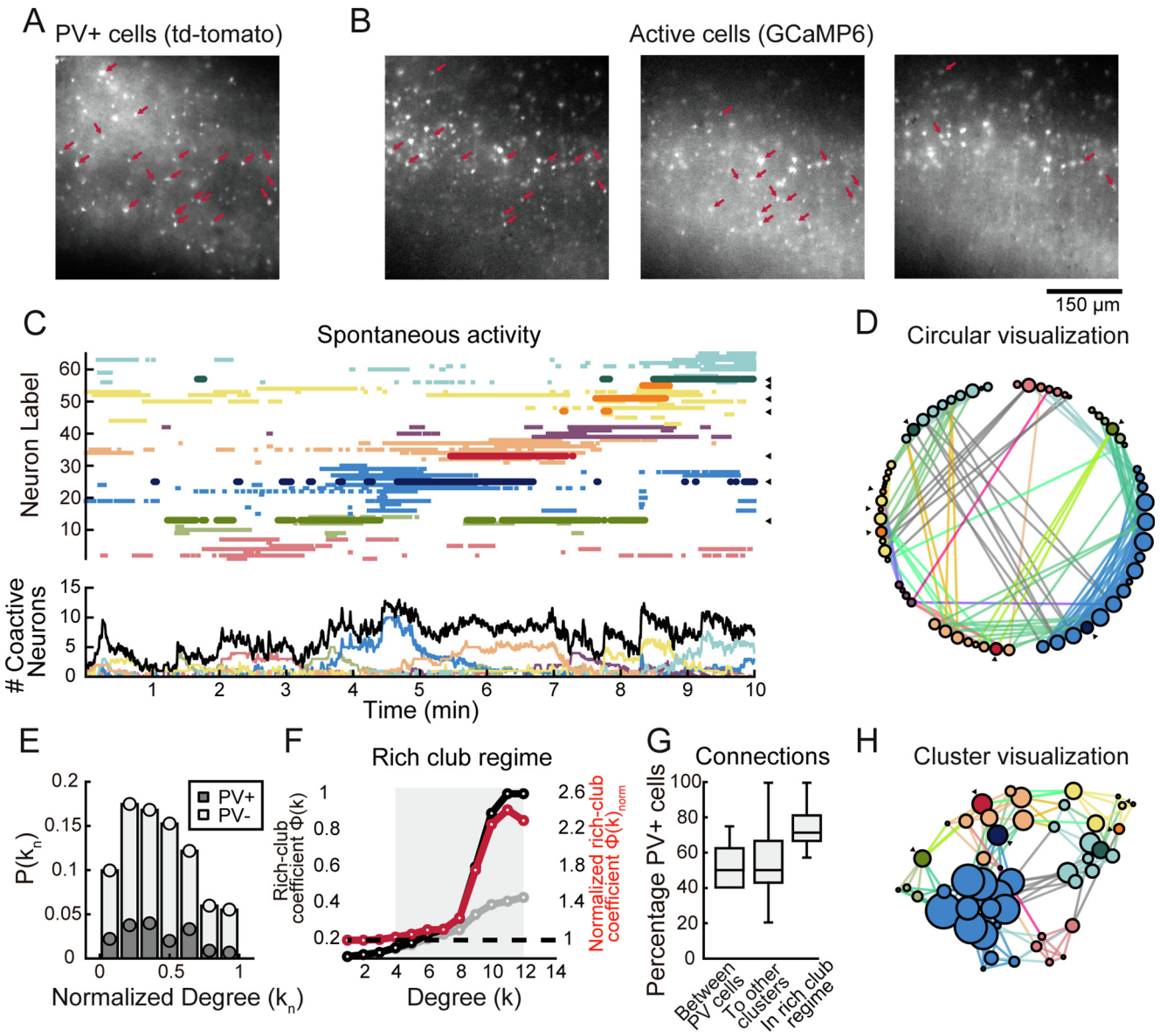

Fig. 3. Participation of the PV+ interneurons in the neuronal ensembles of the mouse motor cortex. **(A)** Photograph of the acquisition field of a calcium imaging video showing neurons marked with td-Tomato (PV+), red arrows indicate interneurons that showed activity in the following panels. **(B)** Photographs at three different moments of the same field illustrated in **(A)**, showing different groups of active neurons expressing GCaMP6f (see Methods). Red arrows indicate interneurons that were marked in **(A)** and that show activity in these frames. **(C)** Raster plot of the spontaneous activity in motor cortex (top). Identified neuronal ensembles are shown in different colors; the activity of PV+ interneurons is indicated with darker color and by the arrowheads on the right. Note that each neuronal ensemble has its own PV+ or subset of PV+ interneurons. At bottom, histogram of the summed whole activity (black) and that of different neuronal ensembles (colored). **(D)** Circular visualization of the microcircuit. Neurons have been sorted according to their ensembles. PV+ interneurons are shown in darker color and with arrowheads. The size of the node denotes the number of connections. **(E)** Distribution of the number of normalized connections of PV+ neurons (dark gray, $n = 70$ neurons) and PV− neurons (light gray, $n = 357$ neurons). **(F)** Rich-club curve for the network shown in **(D)**, the graph shows a significant rich-club behavior of the neural network structure between 4 and 12 functional connections. Normalized rich-club coefficient (red line) increases as a function of k (number of functional connections). The black line shows the rich-club coefficient and the gray line shows the same coefficient for a random network of equal size and similar connectivity distribution **(G)** Percentage of PV+ interneurons that had connections between them, to other ensembles, and percentage located within the rich-club regime ($n = 70$ neurons). **(H)** Microcircuit network exhibiting the nodes with four or more functional connections only (rich-club regime), PV+ neurons are signaled with arrow heads. Note that nodes with higher degrees are not PV+ interneurons. (For interpretation of the references to colour in this figure legend, the reader is referred to the web version of this article.)

et al., 2006; de la Prida et al., 2006). In cortical non-stimulated circuits, this maneuver induced brief and recurrent epileptiform discharges without any stimulation (Huberfeld et al., 2011; Karlócai et al., 2014). According to their duration and recurrence they are similar to interictal epileptiform discharges or IEDs (Brückner and Heinemann, 2000; de Curtis et al., 2012). To observe a movie that compares control spontaneous firing with IEDs activity see Supplementary movie V2. Because our grouping procedure exhibits neuronal ensembles as

those neurons with correlated firing patterns, and because it has been described that firing patterns of PV + interneurons are relatively different to those of PV− neurons during epileptiform discharges (Chang et al., 2018; Levesque et al., 2018), we expected to observe a partial separation between both classes of neurons to better appreciate the class, role and quantity of synchronized neurons. Fig. 4A shows a raster plot that confirms this hypothesis. The temporal structure of control spontaneous ensembles disappears to give rise to brief epileptiform discharges consisting in a sole recurrent ensemble that recruits most active neurons (IEDs). Our grouping method separated this ensemble into two different clusters of neurons whose temporal dynamics are best appreciated in section 4B. The PV+ interneurons previously identified with td-Tomato are shown in darker colors. Note the high presence of interneurons in the group with more prolonged activity (red; 74.2% or 23 interneurons out of 31 neurons in this experiment; and: 76.7 ± 9.1% pooling $n = 9$ slices from different animals; $P < 0.001$; Kolmogorov–Smirnov test). At the bottom of sections 4A and 4B, the coactivity histogram reveals the presence of these IEDs every 19 ± 1.2 s ($n = 9$ slices from nine different animals). Although we do not formally label pyramidal neurons, we know from population descriptions in the rodent cortex that they correspond to about 85% of the neurons that are PV− (Markram et al, 2004; Tremblay et al, 2016), in our results they would correspond mainly to the group of green color, with briefer duration in its activity.

Raster plot activity allowed build a functional connection network (Fig. 4E). A set of parameters was calculated to compare control and IEDs networks (Fig. 4C): PV+ interneurons with correlated activity increased significantly from 6 ± 2.8 to 14 ± 6.2 ($P = 0.024$; Wilcoxon Signed Ranks test in this and other comparisons in this section unless said otherwise; $n = 9$ slices from nine different animals); edges to nodes ratio increased significantly from 2.9 ± 0.6 to 24.5 ± 7.4 ($P = 0.009$; $n = 9$ slices from nine different animals), global clustering coefficient raised from 0.57 ± 0.08 to 0.85 ± 0.04 ($P = 0.009$; $n = 9$ slices from nine different animals), number of neuron groups separated by our method decreased significantly from 4.2 ± 1 to 2.0 ± 0.2 ($P = 0.014$; $n = 9$ slices from nine different animals), the correlation coefficient of neuron activity increased significantly from 0.34 ± 0.04 in the control to 0.48 ± 0.04 during IEDs ($P = 0.013$; $n = 9$ slices from nine different animals), finally, the characteristic path length decreased significantly from 2.82 ± 0.51 in control to 1.44 ± 0.12 during IEDs ($P = 0.009$; $n = 9$ slices from nine different animals). Changes in network parameters reveal a completely different functional architecture in control conditions as compared to IEDs generation in the same tissue (Beggs and Plenz, 2003; Sadovsky and MacLean, 2013; Bullmore and Sporns, 2009; Pérez-Ortega et al., 2016). The extremes of these topological behaviors are: an entirely regular network with predetermined rigid connections and high clustering and the randomly connected network with low clustering but short average path length. At a midpoint, there is the so-called small-world network, which results from the combination of high clustering and short path length. These characteristics have been described in many real-world networks. Small-world networks have also been associated with high levels of topological efficiency, making them competent integrators of information at different scales of study (Watts and Strogatz, 1998; Boccaletti et al., 2006; Feldt et al., 2011). In the networks that we study the small-world-ness changed from ensemble sequences to a rigid repetitive connectivity; both networks where away from a random network (Fig. 3D; Humphries and Gurney, 2008; She et al., 2016), from a small-world-ness value of −0.20 ± 0.14 in control to −1.22 ± 0.06 during IEDs ($P < 0.001$; Kolmogorov–Smirnov test; $n = 9$ slices from nine different animals). Fig. 4E maintains the color code for both clusters within the synchronous ensemble. The activation dynamics of these clusters were aligned with their maximum peaks of activity in each IED (Fig. 4F). Since PV+ interneurons were identified, it is shown that different firing patterns can be attributed to the difference between interneurons (PV+) and other neurons (PV−; Fig. 4G). Half-width durations obtained from Fig. 4F, G showed significant differences: 2.57 ± 0.24 s for the red and 1.58 ± 0.14 s for the green cluster ($P < 0.001$; Kolmogorov–Smirnov test; $n = 9$ slices from nine different animals) in correspondence with PV+ interneurons: 2.57 ± 0.26 s and PV− neurons: 2.07 ± 0.16 s (Fig. 4H; $P = 0.007$; Kolmogorov–Smirnov test; $n = 9$ slices from nine different animals). Therefore, PV+ interneurons have activities with longer durations, suggesting that activation profile of PV+ interneurons during IEDs is different to that of other neurons in the mouse motor cortex. This phenomenon can be seen even if real duration of IEDs is hard to appreciate with calcium imaging due to low temporal resolution: inferred action potentials are within 160 ms image frames. Nevertheless, imaging allows identify PV+ neurons and separate the recurrent ensemble into two clusters with different firing patterns and durations. PV+ interneurons increase their participation in synchronous events (Fig. 4C top-left) in a ratio of 3.4 ± 1.6 ($n = 9$ slices from nine different animals). However, PV− neurons also increase in proportion: 2.9 ± 1.3 ($n = 9$ slices from nine different animals). Thus the proportion of PV+ interneurons with respect to the total number of neurons with significant correlated activity in each experiment was non-significant: 15.5 ± 0.1% in controls and 16.8 ± 1.3% during IEDs.

Extracellular multi-electrode array (MEA) recordings during IEDs

To study IEDs dynamics with higher temporal resolution, extracellular multi-electrode array (MEAs) recordings were made. The same parasagittal slice and protocols used in calcium imaging experiments were employed. The arrangement of the MEA in the slice is shown in Fig. 5A, only the electrodes placed in the cerebral cortex were used for the analysis (red circles). In Fig. 5B cortical electrodes are seen in greater detail. The separation distance between each electrode is 200 μm: it is possible to track events generated on any

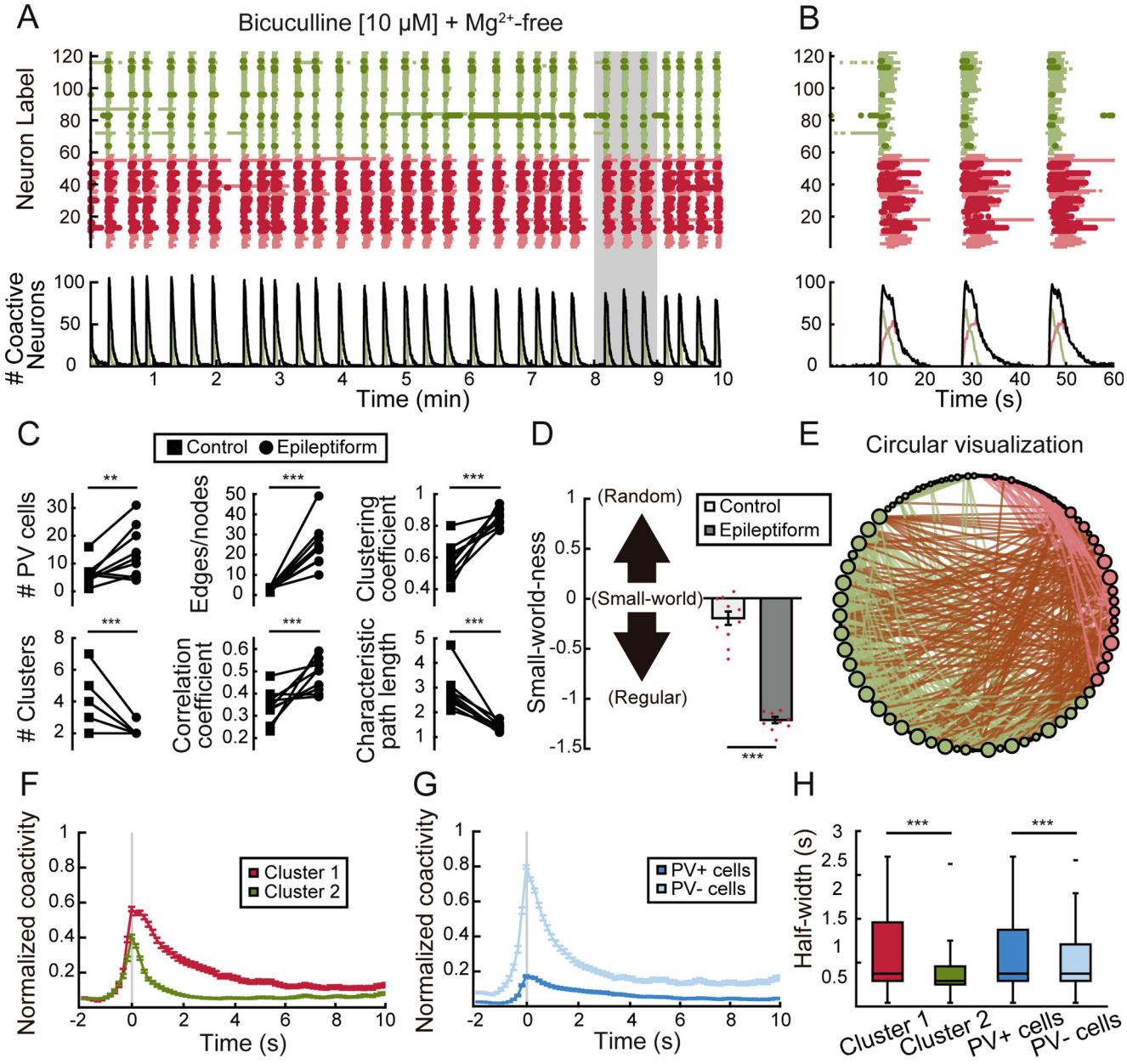

Fig. 4. Participation of PV+ interneurons during interictal epileptiform discharges (IEDs). **(A)** Raster plot of activity after applying 10 μM bicuculline under a virtual Mg^{2+}-free solution: recurrent IEDs are recorded in the slice. Sequence and diversity of neuronal ensembles present during spontaneous activity turns into synchronous events with a single ensemble. The activity of the PV+ interneurons is shown in darker colors. **(B)** Plot of a fraction (shaded) of the raster plot in **(A)**: three epileptiform events are observed. Due to our grouping procedure, most PV+ interneurons (red) appeared as separated to PV− neurons (green), confirming differences in firing patterns. However, some PV+ interneurons also appeared in the green cluster and some PV− neurons appeared in the red cluster of the ensemble. This synchronous event remains active for longer times during IEDs. Bottom in **(A)** and **(B)** show summed activity (black trace), and different time courses for the composing clusters (colored). **(C)** Comparison of a set of differences between control and the IEDs networks: number of PV+ neurons increases significantly while number of discernible neuron clusters decrease during epileptiform activity. Significant differences were found in number of PV+ cells ($P = 0.024$), edges/nodes ratio ($P = 0.009$), clustering coefficient ($P = 0.009$), number of clusters ($P = 0.014$), correlation coefficient ($P = 0.013$) and characteristic path length ($P = 0.009$). Wilcoxon signed-rank test was used in all cases ($n = 9$ slices). **(D)** Small-world-ness of the spontaneous and epileptiform networks, respectively. Values close to '0' indicate similarity to a small-world network, while '1' or '−1' denote random and regular networks, respectively ($P < 0.001$; Kolmogorov–Smirnov test; $n = 9$ in each sample). **(E)** Circular visualization of the network formed with raster plot shown in A, the increase in functional connections make it appear as a regular network. **(F, G)** Normalized coactivity of the grouped clusters within the ensemble. Grouped from several experiments and aligned to the peak of maximum activity (zero) of the IEDs. **(H)** Half-width duration of the plots shown in **(F, G)** red cluster ($P < 0.001$) and identified PV+ interneurons ($P = 0.007$) had longer lasting activity during IEDs (in both cases Kolmogorov–Smirnov test, $n = 256$ IEDs from $n = 9$ slices). (For interpretation of the references to colour in this figure legend, the reader is referred to the web version of this article.)

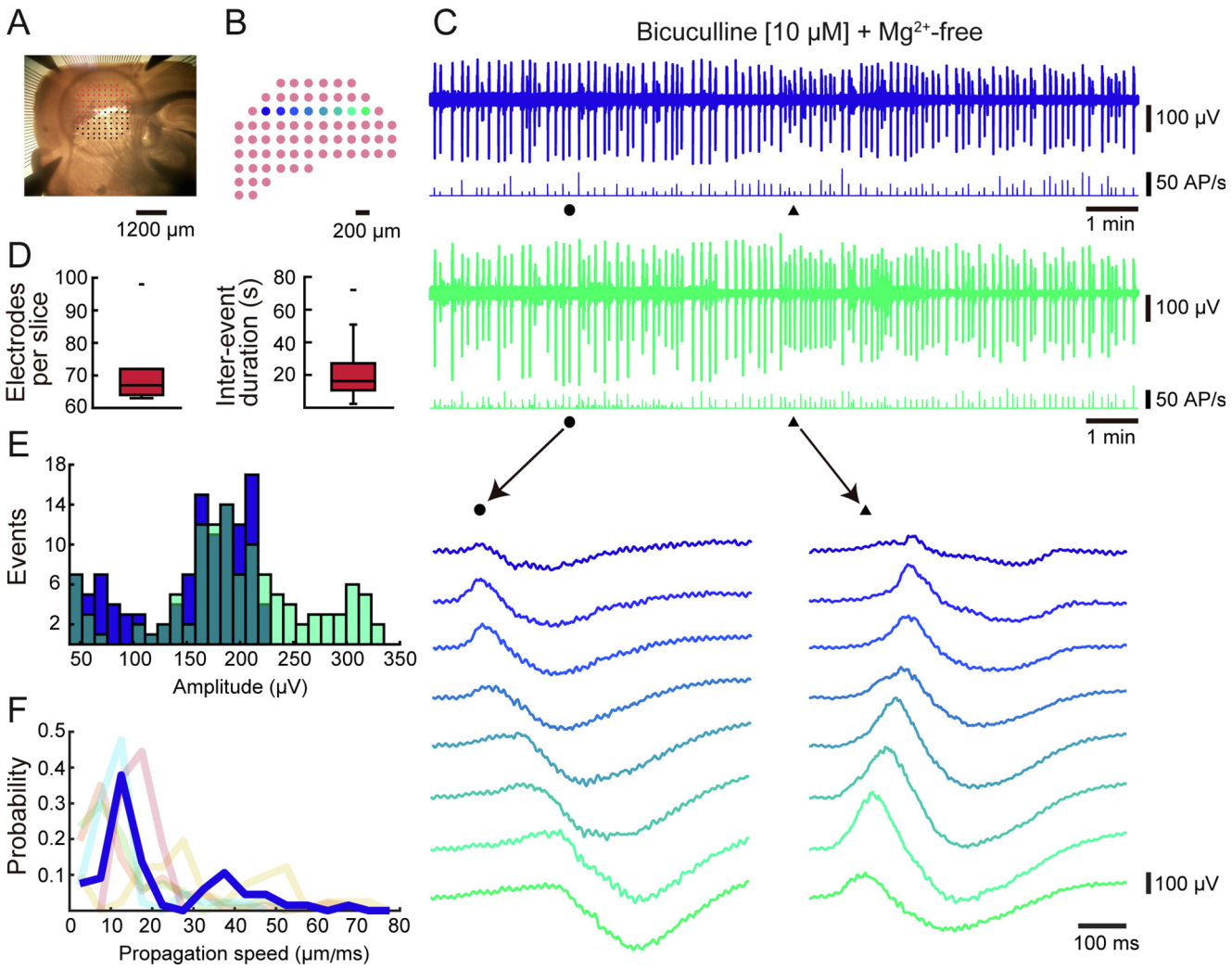

Fig. 5. Extracellular multi-electrode array (MEA) recordings during interictal epileptiform discharges (IEDs). **(A)** Photograph showing the disposition of the MEA in the slice, in the present work only the electrodes that were in the cerebral cortex were considered (red dots). **(B)** Scheme of the electrodes used to characterize the IEDs shown in the following panels. **(C)** Extracellular recordings were done after applying 10 µM bicuculline in virtual Mg^{2+}-free solution. Top, local field potential of IEDs (LFP, low-pass filter < 100 Hz) from electrodes according to color code shown in **(B)**. The recordings shown correspond to the opposite sides of the electrodes line. The circle and the triangle correspond to the instants of time analyzed over the entire line of electrodes. Frequency of action potentials (see below) is shown in the lower line of each recording. Recordings at bottom show IEDs spreading in both directions. **(D)** Left, number of electrodes considered in each slice (n = 6 slices from different animals). Right, inter-event duration between recurrent IEDs (n = 300 events from different animals). **(E)** Amplitude distribution for all IEDs (LFPs) in the recordings shown at **(C)** top. **(F)** Distribution of speed propagation of IEDs in each slice (light colors), blue line correspond to slice shown in **(C)**. (For interpretation of the references to colour in this figure legend, the reader is referred to the web version of this article.)

electrode and directions of wave spreading across the slice. A row of electrodes is also indicated following a color code used in the subsequent panels. Fig. 5C above and middle show local field potential (LFP, low-pass filter < 100 Hz) and firing rate of IEDs recorded by color-coded electrodes; electrodes positioned at the ends of the row. Unitary firing rate (see below) measured at electrodes increases in correlation with synchronous IEDs. Bottom of Fig. 5C shows recordings from the entire row of electrodes (Fig. 5B) taken at two different times indicated by black circles and triangles on the top panel. IEDs (LFPs) could be seen propagating locally in both directions. Fig. 5D left, the number of electrodes considered in each experiment is reported: 72 ± 10 electrodes (n = 6 slices from six different animals). Fig. 5D right, the duration between inter IEDs intervals was 22 ± 1.96 s (n = 300 events from six different animals; non-significantly different to that found with calcium imaging – see above). Distribution of IEDs identified by LFPs is shown in Fig. 5E (n = 300 events from six different animals), the average voltage amplitude of each identified IED at each electrode was 180 ± 48 µV (360 electrodes and 1734 events). The propagation speed of IEDs in each slice was calculated (Fig. 5F), the highlighted color curve corresponds to the data of the slice shown in C. Propagation speed was 15.3 ± 2.4 µm/s (n = 6 slices from six different animals). We found IEDs with similar spatial and temporal attributes spreading in different directions in each slice (Serafini et al., 2016). These

experiments showed that IEDs identified electrophysiologically by LFPs closely correspond to those identified by calcium imaging. The fact that they propagate without a predominant direction being initiated in any electrode suggests that they are locally generated, away from long range interferences.

Neuronal activity during the occurrence of IEDs

After obtaining IEDs in a stable manner, we studied individual units with MEA electrodes. To observe control spontaneous firing in raw data before using a grouping method see Supplementary Fig. S2. Fig. 6A shows an example of a multi-unit recording with extracellular action potentials and a burst from one MEA electrode (bandpass filter 500–5000 Hz). Identified action potentials were aligned 1 ms before and 2 ms later with respect to their most negative voltage point in the recordings (Fig. 6B). Individual units were extracted according to their shapes (see Experimental procedures; gray and blue; Fig. 6C) and used to build raster plots with individual units (Fig. 6D, E). The number of individual units per electrode was 1.2 ± 0.8 (n = 360 electrodes, n = 6 slices from six different animals). Spikes were sorted by our grouping method (see Material and Methods) to see whether neuronal classes could be separated. Synchronous activity during an IED clearly shows a synchronous ensemble with two clusters with different firing patterns and durations. Real spikes obtained with higher temporal resolution (MEA) closely resemble inferred spikes obtained with calcium imaging (Fig. 6D, E). In addition, simultaneous LFPs recordings were obtained (Fig. 6F, G). The LFP components in an IED were: an inter-ictal spike followed by a slow wave and late oscillations mainly corresponding to the cluster that lasts longer. The whole event lasts about 3.5 ± 0.18 s (n = 1734 events, n = 6 slices from six different animals). Representative spectrograms are shown (Fig. 6H, I), note gamma band during the spike and theta and alpha bands corresponding to late oscillations (Huberfeld et al., 2011). Action potentials coactivity (Fig. 6J , K) shows a longer duration in the red cluster, as obtained in calcium imaging experiments. Basically, these experiments showed that IEDs analyses yield similar results using real unitary action potentials (MEAs) and inferred action potentials (calcium imaging).

Morphological and electrophysiological characterization of neurons recorded from different clusters during IEDs

Whole-cell recordings were performed in layers 5–6 of mice motor cortices in PV+ and PV− neurons both in control conditions and after inducing IEDs with 10 μM bicuculline under Mg^{2+}-free conditions. Fig. 7A shows the morphology of a pyramidal neuron intracellularly labeled with streptavidin-Cy3 conjugated with biocytin and recorded during resting control conditions. Voltage responses to the application of hyperpolarizing and depolarizing current pulses at the soma (Fig. 7B) and its corresponding current voltage relationship (I–V plot; Fig. 7C). The input resistance for a sample of PV− neurons with the same characteristics was 328 ± 68 MΩ (n = 12 neurons from 12 different animals). During the synchronous stage of an IED, the firing of this same neuron without stimulation (Fig. 7D) exhibited a depolarizing shift and a train of spikes. All neurons in this sample appeared in the brief duration clusters during IEDs. Fig. 7E shows a PV+ interneuron (td-Tomato viral transfection plus intracellular labeling with streptavidin-FITC conjugated with biocytin). The extensive dendritic arbor excludes a pyramidal cell. Voltage responses (top) to current steps (bottom; Fig. 7F) and corresponding I-V plot (Fig. 7G) yield an average input resistance of 204 ± 60 MΩ (mean ± SEM, n = 7 neurons from seven different animals), significantly different to that measured from pyramidal neurons (P = 0.034; Kolmogorov–Smirnov test; n_1 = 7 PV+ cells; n_2 = 12 PV− neurons with pyramidal cells morphology, all cases from different animals). A depolarizing shift and a more prolonged train of spikes (Fig. 7H) reaching higher frequencies (see Fig. 8D) were commonly found in the sample of PV+ interneurons. n = 6 out of seven neurons of this sample were recorded within longer duration clusters during IEDs.

Differences in the duration of synchronous ensemble clusters during IEDs

The two clusters identified in MEA recordings within IED events present different activation profiles, firing patterns and durations. Coactivity of these clusters during single IEDs is illustrated in Fig. 8A (color code of as in Fig. 6). Half-width duration for the red cluster was 0.38 ± 0.02 s and it was 0.33 ± 0.05 s for the green cluster (Fig. 8B; P < 0.001; Kolmogorov–Smirnov test; n = 306 from six different animals in both cases). In the calcium imaging experiments, most of the labeled PV+ interneurons had a more prolonged activity than the other neuronal types, mainly coinciding with the pattern of activity of the red cluster. Fig. 8C shows duration of action potentials trains of individually recorded neurons using the whole-cell technique: 1.07 ± 0.49 s for PV+ interneurons, significantly longer duration than that measured in pyramidal cells: 0.49 ± 0.53 s (P < 0.001; Kolmogorov–Smirnov test; n_1 = 119 PV+ neurons events; n_2 = 354 PV− trains of spikes, all cases from different animals). This phenomenon is observed in Fig. 7D where pyramidal neurons have a much briefer bursts than PV+ interneurons. The firing rate of the action potentials during IEDs (Fig. 8D) in PV+ interneurons was 61.9 ± 12.6 Hz, significantly higher than that shown by pyramidal neurons: 33.4 ± 4.8 Hz (P < 0.001; n_1 = 7 PV+ cells; n_2 = 12 pyramidal cells; Kolmogorov–Smirnov test, all cases from different animals) supporting frequencies reached during spectrograms. The coefficient of variation (Fig. 8E) measured for PV+ cells: 0.37 ± 0.06 and pyramidal neurons: 0.67 ± 0.12 was significantly different (P = 0.004; n_1 = 7 PV+ cells; n_2 = 12 pyramidal cells; Kolmogorov–Smirnov test, all cases from different animals). Inter-event durations measured from peak to

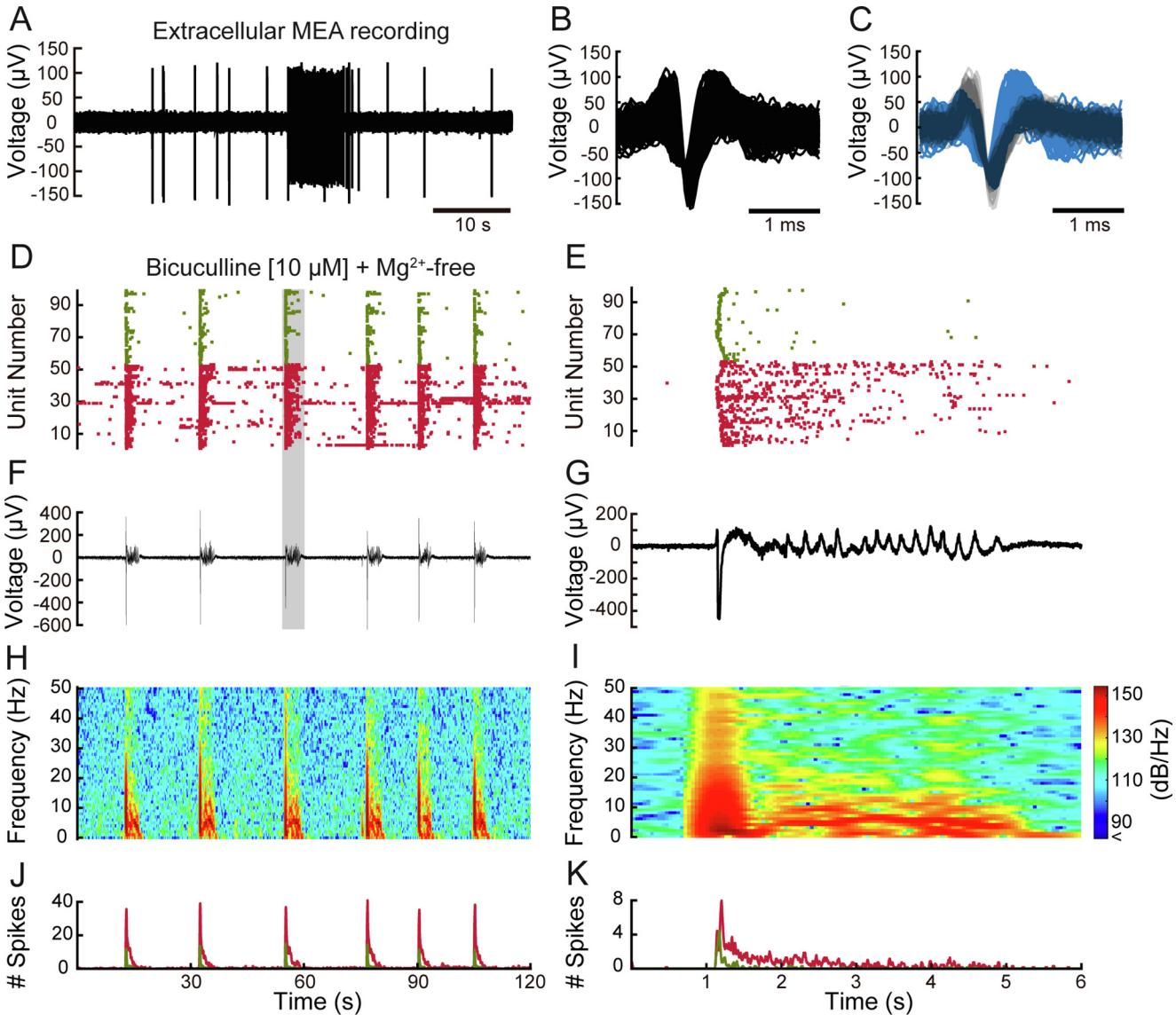

Fig. 6. Unitary activity during the occurrence of IEDs. **(A)** Example of a multiunit recording with extracellular action potentials and a burst from one MEA electrode (bandpass filter 500–5000 Hz). **(B)** Spike waveforms detected from **(A)**, these events were detected as changes in voltage that exceeded a threshold of six SD of global electrode signal (see Experimental procedures). **(C)** Individual units extracted from **(B)** (see Experimental procedures); two units were identified in this electrode (light blue and gray, superposition is dark blue). **(D, E)** Raster plot of recurrent IEDs and magnification of one event in **(E)** (shaded area in **(D)**). Each row denotes activity exhibited by individual units (recorded action potentials) during IEDs, after applying 10 μM bicuculline under Mg^{2+}-free conditions. Ca^{2+}-imaging results (inferred action potentials in Fig. 4**(A)**) are confirmed by MEAs (real action potentials): the neurons fire in near synchrony into one ensemble which is grouped into two clusters by their different correlated firing patterns. One characteristic that defines clusters is their duration: activity lasts more in one of them (red). **(F, G)** Local field potential (LFP, low-pass filter < 100 Hz) simultaneously recorded during neuronal firing. Magnification **(G)** shows the components of the LFP: an inter-ictal spike followed by a slow wave and late oscillations that mostly correspond to activity in the ensemble that lasts longer. **(H, I)** Spectrograms of the recordings shown in **(F, G)**. **(J, K)** Coactivity of individual neurons with a time interval of 5 ms, separated according to identified clusters, note different time courses confirming findings using Ca^{2+}-imaging and inferred spikes. (For interpretation of the references to colour in this figure legend, the reader is referred to the web version of this article.)

peak of maximal activity IEDs obtained with the different experimental protocols were similar (Fig. 8F; $P = 0.54$; Kruskal–Wallis ANOVA test; $n_1 = 111$ PV+ interneurons inter-events; $n_2 = 333$ pyramidal neurons inter-events; $n_3 = 187$ calcium imaging inter-events; $n_4 = 300$ MEA inter-events, all cases from different animals). Thus, experiments showed similar results with all techniques used.

DISCUSSION

Original findings of the present work are: (1) Resting, non-stimulated, cortical tissue *in vitro* have a spontaneously generated activity which consist in temporal sequences of neuronal ensembles: groups of neurons with strongly correlated spatiotemporal activity patterns, demonstrated with pair to pair correlations in control

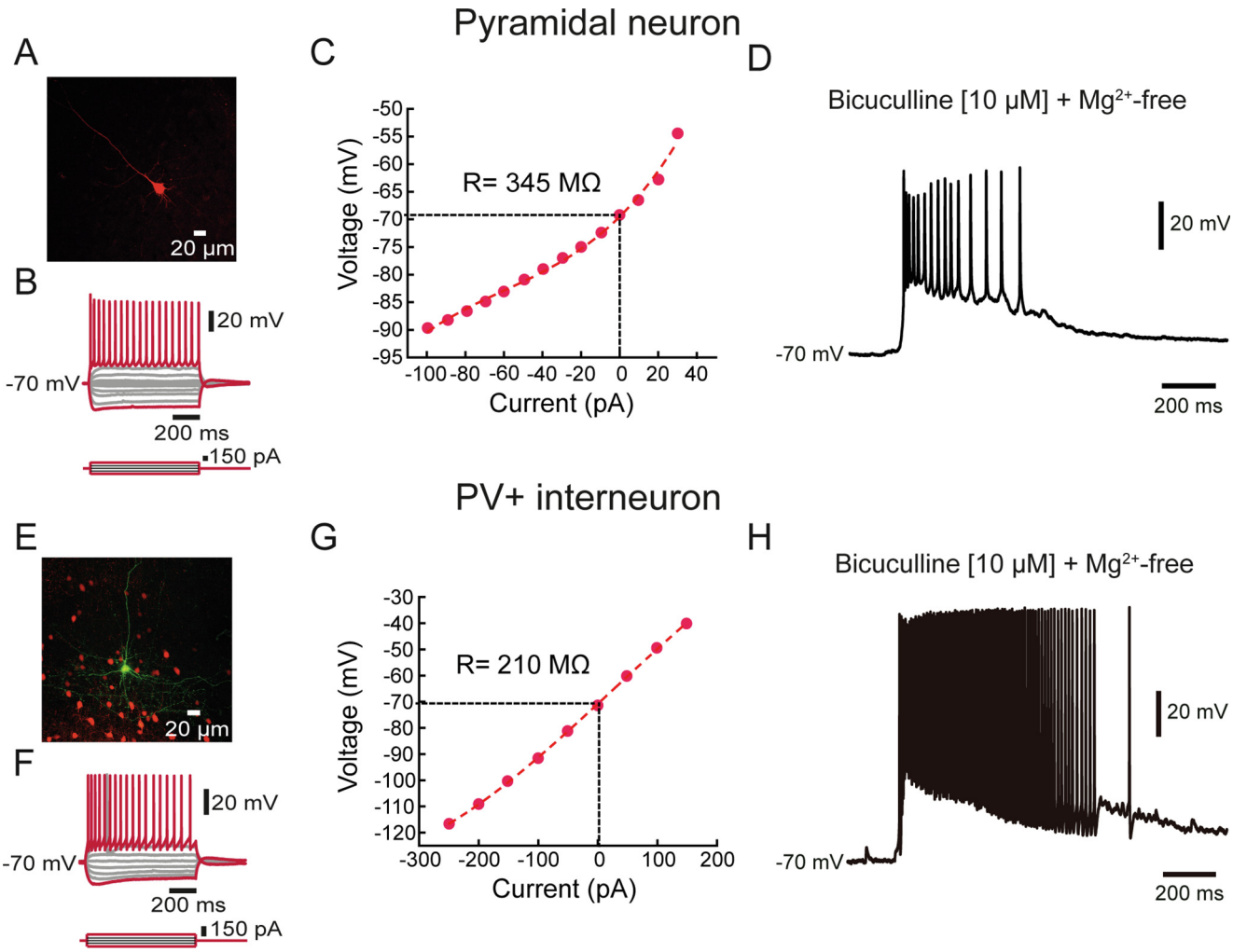

Fig. 7. Morphological and electrophysiological characterization of two main classes of neurons recorded before and during interictal epileptiform discharges. **(A)** Morphology of a pyramidal neuron intracellularly labeled with streptavidin-Cy3 conjugated with biocytin (red). **(B)** Voltage responses (top) to the application of depolarizing and hyperpolarizing current pulses (bottom) at the soma of the same cell. Recorded in control conditions. **(C)** Current-voltage relationship (I–V plot) of the neuron shown in **(A)**. **(D)** Depolarizing shift plus train of spikes during the synchronous stage of an IED under 10 µM bicuculline and Mg^{2+}-free conditions of the same cell. **(E)** Morphology of an interneuron identified as PV+ by viral transfection with td-Tomato (red) and intracellularly labeled with streptavidin-FITC conjugated biocytin (yellow). **(F)** Voltage responses (top) after application of depolarizing and hyperpolarizing current pulses (bottom) at the soma of the same cell. Recorded in control conditions. **(G)** I–V plot of the neuron shown in **(F)**. **(H)** Depolarizing shift and train of spikes of the same PV+ interneuron recorded during the synchronous stage of an IED in 10 µM bicuculline and Mg^{2+}-free conditions. Note lower input resistance (cf. I–V plots), higher firing frequency and longer duration of firing as compared with **(D)**. (For interpretation of the references to colour in this figure legend, the reader is referred to the web version of this article.)

conditions. There is some neuronal overlapping between neuronal ensembles (Carrillo-Reid et al., 2009; Dechery and MacLean, 2017). (2) When active, most neuronal ensembles are accompanied by the firing of at least one PV+ interneuron. Because our sampling comprises a few dozen of neurons, it is possible that observed ensembles are samples of larger neuronal groups below and above of our two dimensional plane of view, thus this observation may be an underestimation. However, this view suffice to observe the recurrent temporal sequences (Buzsáki, 2010; Dechery and MacLean, 2017). (3) Network analysis showed that this control default activity *in vitro* is similar to a small-world configuration with a few neurons having great connectivity and forming a rich club. Interestingly, most connected neurons were PV-, most probably pyramidal neurons (Fornito et al 2016). (4) The blockade of GABA transmission with bicuculline in a virtual Mg^{2+}-free extracellular medium (Hongo et al 2015) suffice to remodel the network to generate brief recurrent epileptiform discharges without stimulation. Due to their duration they are similar to interictal epileptiform discharges or IEDs (Brückner and Heinemann, 2000; de Curtis et al., 2012). They are seen as coactivity of PV+ and PV− neurons forming a large ensemble, both with inferred action potentials after calcium imaging and with real action potentials after MEA recordings, forming an initial synchronicity with high frequency followed by brief after-discharges. The initial peak of coactivity corresponds to the initial interictal spike in the LFP, and after-discharges correspond to its slow oscillations. (5) The importance of fast spiking interneurons activity (FSIs or PV+ cells) in these synchronous events was done with

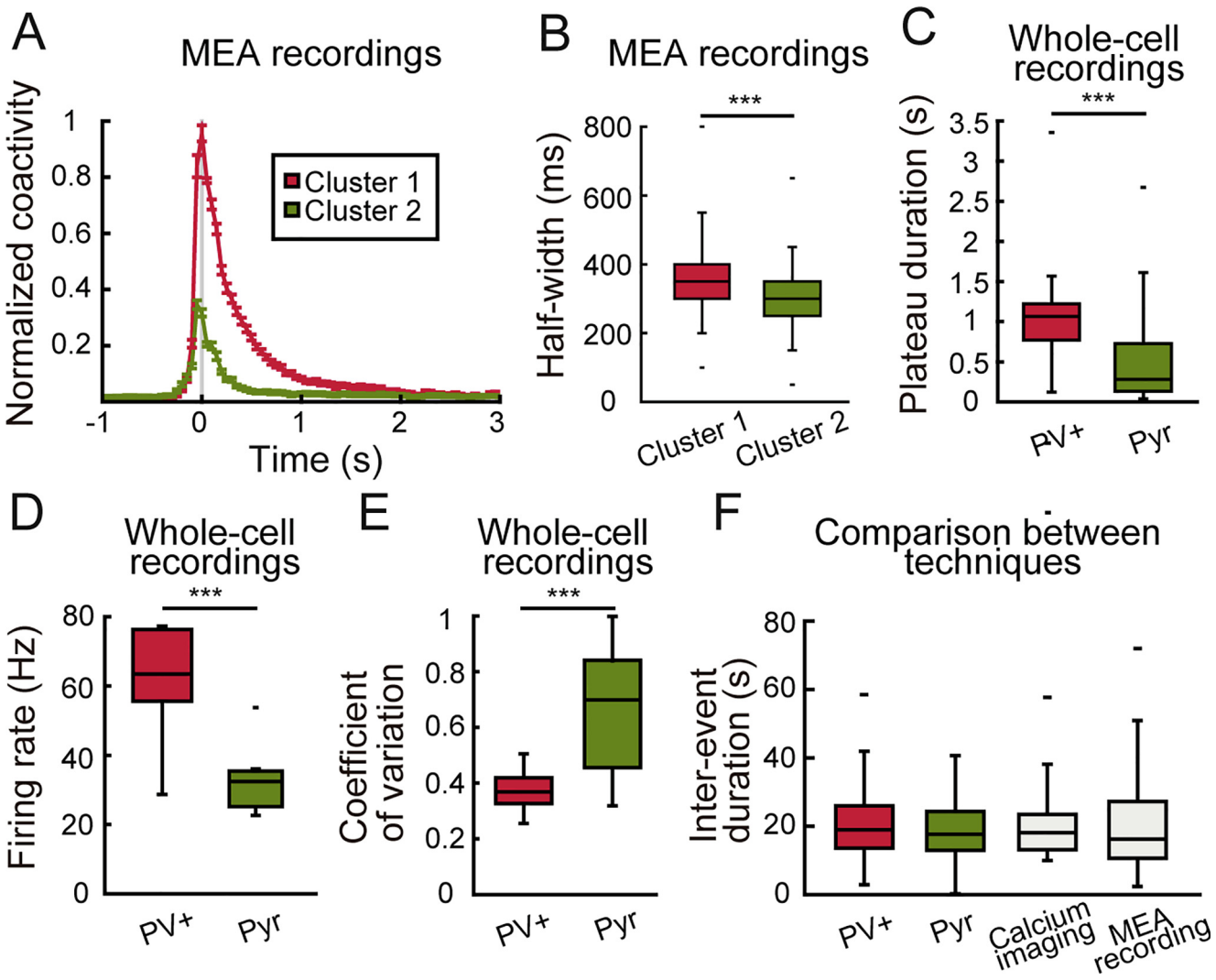

Fig. 8. Differences in the duration of clusters making up IEDs. **(A)** Normalized coactivity of multi-units clusters within IEDs separated by their differing firing patterns and aligned to their maximal peak of coactivity at time zero (MEA recordings; color code in previous figures is followed). **(B)** Half-width (duration at half coactivity amplitude) shows a cluster exhibiting longer duration (red) during IEDs, similar to results obtained with calcium imaging experiments ($P < 0.001$; $n = 306$ in both cases; Kolmogorov–Smirnov test). **(C)** Difference in duration of action potentials trains of individually recorded interneurons and pyramidal neurons (whole-cell recordings). Similar to results with calcium imaging, interneurons units remain active for longer periods during IEDs (MEA recordings; $P < 0.001$; $n1 = 119$ PV+ events; $n_2 = 354$ PV− events; Kolmogorov–Smirnov test). **(D)** Firing rate of action potentials of PV+ interneurons during IEDs was higher than the rate reached by identified pyramidal neurons (Whole-cell recordings $P < 0.001$; $n_1 = 7$ PV+ cells; $n_2 = 11$ pyramidal cells; Kolmogorov–Smirnov test). **(E)** Coefficient of variation was significantly higher in pyramidal neurons with respect to PV+ cells ($P = 0.004$; $n_1 = 7$ PV+ cells; $n2 = 11$ pyramidal cells; Kolmogorov–Smirnov test). **(F)** Mean inter-event duration between recurrent IEDs ($P = 0.54$; $n_1 = 111$ putative PV+ inter-events; $n_2 = 333$ putative pyramidal inter-events; $n_3 = 187$ calcium imaging inter-events; $n_4 = 300$ MEA inter-events; Kruskal–Wallis test). (For interpretation of the references to colour in this figure legend, the reader is referred to the web version of this article.)

identified neurons in PV-Cre mice. However, PV− (mainly glutamatergic) neurons also participate. (6) Network analysis generated a recurrent repetitive network with many functional connections as compared to the controls. As expected, this kind of network tended to leave the small-world configuration and tended to adopt that of a regular network (Watts and Strogatz, 1998). (7) Targeted whole cell recordings in current clamp confirmed that identified PV+ neurons have action potentials trains with higher frequency and longer duration than those of pyramidal cells. This is why, in the present conditions, after-discharges are basically due to interneurons.

Network default configuration in resting cortical tissue

Calcium imaging experiments with single cell resolution demonstrated the long-standing hypothesis that a temporal sequence of cortical neuronal ensembles is generated spontaneously in non-stimulated cortical tissue *in vitro* (Hebb, 1949; Abeles, 1991; Beggs and Plenz, 2004; Ikegaya et al., 2004; Luczak et al., 2007; Pastalkova et al., 2008; Dechery and MacLean, 2017). Therefore these phenomena represents a basic structured activity of mice motor cortex at rest or without stimulation and long range influences (Luczak et al., 2007), in

need of further study. In our experimental conditions this resulted in a stable form of spontaneous activity in mice motor cortex, without the need of stimulation and without long range influences. Intersections between ensembles suggest some neuronal overlapping (Carrillo-Reid et al., 2009; Dechery and MacLean, 2017). During this spontaneous activity, each neuronal ensemble has the association of PV+ interneurons, almost ensemble by ensemble. From the various mechanism to explain these sequences two are pertinent here: (1) Synchronized glutamatergic neurons excite the next ensemble in a recurrent sequence of a class of feed-forward circuit (Hebb, 1949; Abeles et al., 1991; Aertsen et al., 1996; Reyes, 2003; Fries, 2005; DeMarse et al., 2016). (2) Inhibitory neurons are necessary to inhibit the non-firing ensembles, and the activity and number of neurons in their own ensembles in an excitatory-inhibitory interplay (Sanchez-Vives and McCormick, 2000; Cossart et al., 2003; Litvak et al., 2003; Grillner et al., 2005). Here we show experimental evidence that both mechanisms do not exclude each other.

PV+ neurons have a characteristic pattern of activity within the circuit. Because our grouping procedure depends on firing pattern correlation, this result suggest that different PV+ neurons adapt their firing pattern to that of their PV− companions, suggesting a precise role in each ensemble. Because both PV+ or FSIs and PV− (mostly pyramidal neurons) increase during GABAergic blockade and collapse temporal sequences of neuronal ensembles found in the control, the need of interneurons to regulate control temporal sequences seems important, both to inhibit non-firing ensembles and to limit the number of neurons in their own ensembles. Otherwise a single repetitive ensemble firing once and again takes place.

The degree distribution of the PV+ and PV− neurons are similar, indicating that there is an equal probability of finding one of these types of neurons as hubs in the network. However, the largest proportion of PV− neurons (most probably pyramidal neurons) causes us to find these types of neurons as the more common hubs in agreement with rich-club metrics. These experimental evidences suggest that feed-forward sequences driven by pyramidal neurons are controlled by inhibition to generate ordered sequences. PV+ interneurons and their corresponding ensembles were closely linked to the highly connected hubs. In this scheme, other interneuron classes need to be studied using a similar framework.

Remodeling of cortical functional architecture following GABAergic blockade

The exact cellular machinery that generates the temporal sequences of neuronal ensembles in the resting cortical circuitry is unknown, however, it should be completely remodeled after removing the important component given by GABAergic inhibition. By blocking GABAergic transmission, a non-stimulated resting cortical tissue is capable to reconfigure itself from a temporal sequence of neuronal ensembles with sparse and ordered PV+ interneurons participation, to a single recurrent ensemble that repeats itself regularly. Network analysis proved this remodeling since the small-world configuration seen in the control was transformed to a regular network with many more correlation links and a single synchronous ensemble. We identified PV+ neurons in calcium imaging experiments with td-Tomato, and lately we inferred their activity together with that of PV− neurons using GCaMP6f under the synapsin promoter. Our grouping method clearly divided the IED ensemble into two clusters with different firing patterns, thus destroying the similar correlation between PV+ and PV− neurons observed in the control ensembles. One of these clusters possessed more interneurons and lasted during more prolonged times. Real unitary action potentials obtained with MEA showed the same result: two clusters one lasting more than the other. It was true that the number of interneurons increased during these events, but PV− neurons also increased so that their proportion within the active and synchronous neuronal population remained the same, discarding that PV+ interneurons have a predominant role during this type of discharges. The fact that both PV+ and PV− neurons fired at the same initial time window is probably due to the lack of GABAergic inhibition. Thus, GABA transmission is not needed to reach this stage or to activate these neuronal populations or to generate the silent period between the epileptiform discharges. However, in no case we could see the development of an ictal-like event, suggesting the need of GABAergic transmission to reach that stage (Sessolo et al., 2015; Khoshkhoo et al., 2017; Chang et al., 2018). The sole blockade of GABA transmission do not produce them without stimulation (Bekenstein and Lothman, 1993; Jirsa et al., 2014; Zaitsev, 2017).

These experiments also demonstrate that synchronization of GABAergic and glutamatergic neurons do not need GABAergic transmission but are favored by the lack of it. Alternation between PV+ and PV− neurons, such as that seen with the 4-AP model (Levesque et al., 2018) is not seen perhaps because GABAergic transmission has been blocked, but this has to be proven with the present experimental conditions in future studies. In addition, the fact that these events could be maintained for several minutes without entering an ictal-like event show that IEDs are not due to GABAergic transmission, at least that coming from ligand-gated $GABA_A$ receptors. This network behavior is totally reversible to the one shown in Fig. 1 (see Supplementary Fig. S1).

Recordings of real action potentials with MEAs closely resembled those obtained with inferred action potentials obtained with calcium imaging: IEDs-like events consists in a synchronous high frequency event reaching the gamma band and coinciding with the interictal main spike recorded as LFP, followed by lower spike frequencies coinciding with the slow wave in the LFP. Spikes firing from one of the clusters after the initial synchronous event had frequencies within theta and

alpha bands coinciding with late oscillations in the LFP. According to calcium imaging experiments most spikes in the red cluster should correspond to FSIs or PV+ interneurons.

To completely be sure of this inference, we individually recorded neurons from these different clusters during these events and anatomically identified them with immunocytochemistry. Whole-cell current-clamp experiments before and during IEDs synchronization confirmed that the grouping method used in both calcium imaging and MEA recordings did distinguish between pyramidal neurons (most PV−) and PV+ interneurons firing patterns, making it easy to count their participation and attesting their roles during IEDs synchronization by separating them into two clusters within the same event. By measuring the duration of their trains of action potentials we proved that PV+ neurons fire during more prolonged times.

In conclusion, resting control or non-stimulated mouse motor cortex *in vitro* spontaneously generate a patterned network activity consisting in temporal sequences of neuronal ensembles, which persists in a recurrent way without stimulation and long range influences. Each neuronal ensemble might be accompanied by a PV+ or FSI. The configuration of this circuit is similar to a small-world network. Rich club metrics yield that most connected hub neurons are PV− favoring the hypothesis of feed-forward propagation through pyramidal cells. However, ensembles with PV+ neurons are connected to these hubs, and when ligand-gated fast GABA transmission is blocked, the temporal sequences of ensembles collapses into a unique recurrent ensemble, suggesting that inhibition is necessary to control spontaneous activity. The resulting ensemble has the duration and electrophysiological characteristics of brief recurrent IEDs composed by the coactivity of both PV− and PV+ neurons, suggesting that fast GABA transmission commonly impedes its occurrence. These synchronous events are clearly divided into two clusters one of them with more prolonged firing than the other because it is mainly composed with PV+ neurons. Because an ictal-like event was not recorded after several minutes of IEDs recording, we conclude that perhaps a different stimulus and/or fast GABA transmission are necessary for its appearance, making this preparation ideal to study both cortical spontaneous activity mechanisms and its transformation into brief epileptiform discharges.

ACKNOWLEDGEMENTS

Authors thank Antonio Laville and Ariadna Aparicio-Juárez for technical support, Claudia Rivera-Cerecedo, Héctor Alfonso Malagón-Rivero and Xochitl Ayala for their help in animal care facility. Ana María Escalante and Francisco Pérez Eugenio for fixing computational incidents. This work was supported by public grants CONACYT Frontera 57 FON.INS. 29-10, DGAPA-UNAM: IN202920 to J.B. and IN203020 to E.G. Miguel Serrano-Reyes is a student from the Programa de Doctorado en Ciencias Biomedicas, Universidad Nacional Autónoma de México (UNAM), and received doctoral fellowship 375821 from CONACYT. Data in this work are part of his doctoral dissertation.

AUTHOR CONTRIBUTIONS

Miguel Serrano-Reyes: Study conception and design, Acquisition of data, Analysis and interpretation of data, Drafting of manuscript. Brisa García-Vilchis: Acquisition of data. Rosa Reyes-Chapero: Acquisition of data. Dagoberto Tapia: Acquisition of data. Elvira Galarraga: Drafting of manuscript, Critical revision. José Bargas: Study conception and design, Interpretation of data, Drafting of manuscript, Critical revision.

DECLARATIONS OF INTEREST

None.

REFERENCES

Abeles M (1991) Corticonics: neural circuits of the cerebral cortex. Cambridge, UK: Cambridge University Press.

Aertsen A, Diesmann M, Gewaltig MO (1996) Propagation of synchronous spiking activity in feedforward neural networks. J Physiol Paris 90(3–4):243–247. https://doi.org/10.1016/s0928-4257(97)81432-5.

Arias-García MA, Tapia D, Laville JA, Calderón VM, Ramiro-Cortés Y, Bargas J, Galarraga E (2018) Functional comparison of corticostriatal and thalamostriatal postsynaptic responses in striatal neurons of the mouse. Brain Struc Funct 223:1229–1253. https://doi.org/10.1007/s00429-017-1536-6.

Avoli M, de Curtis M (2011) GABAergic synchronization in the limbic system and its role in the generation of epileptiform activity. Prog Neurobiol 95:104–132. https://doi.org/10.1016/j.pneurobio.2011.07.003.

Avoli M, Panuccio G, Herrington R, D'Antuono M, de Guzman P, Lévesque M (2013) Two different interictal spike patterns anticipate ictal activity in vitro. Neurobiol Dis 52:168–176. https://doi.org/10.1016/j.nbd.2012.12.004.

Avoli M, Jefferys JGR (2016) Models of drug-induced epileptiform synchronization in vitro. J Neurosci Methods 260:26–32. https://doi.org/10.1016/j.jneumeth.2015.10.006.

Beggs JM, Plenz D (2004) Neuronal avalanches are diverse and precise activity patterns that are stable for many hours in cortical slice cultures. J Neurosci 24(22):5216–15129. https://doi.org/10.1523/JNEUROSCI.0540-04.2004.

Bekenstein JW, Lothman EW (1993) Dormancy of inhibitory interneurons in a model of temporal lobe epilepsy. Science 259 (5091):97–100. https://doi.org/10.1126/science.8093417.

Binnie CD (2003) Cognitive impairment during epileptiform discharges: is it ever justifiable to treat the EEG? Lancet Neurol 2:725–730. https://doi.org/10.1016/s1474-4422(03)00584-2.

Boccaletti S, Latora V, Moreno Y, Chavez M, Hwanga DU (2006) Complex networks: structure and dynamics. Phys Rep 424:175–308. https://doi.org/10.1016/j.physrep.2005.10.009.

Bruno AM, Frost WN, Humphries MD (2015) Modular deconstruction reveals the dynamical and physical building blocks of a locomotion motor program. Neuron 86:304–318. https://doi.org/10.1016/j.neuron.2015.03.005.

Brückner C, Heinemann U (2000) Effects of standard anticonvulsant drugs on different patterns of epileptiform discharges induced by 4-aminopyridine in combined entorhinal cortex-hippocampal slices. Brain Res 859:15–20. https://doi.org/10.1016/s0006-8993(99)02348-3.

Bullmore E, Sporns O (2009) Complex brain networks: graph theoretical analysis of structural and functional systems. Nat Rev Neurosci 10:186–198. https://doi.org/10.1038/nrn2575.

Buzsáki G (2010) Neural syntax: cell assemblies, synapsembles, and readers. Neuron 68:362–385. https://doi.org/10.1016/j.neuron.2010.09.023.

Buzsáki G, Tingley D (2018) Space and Time: The Hippocampus As A Sequence Generator. Trends Cogn Sci 10:853–869. https://doi.org/10.1016/j.tics.2018.07.006.

Cammarota M, Losi G, Chiavegato A, Zonta M, Carmignoto G (2013) Fast spiking interneuron control of seizure propagation in a cortical slice model of focal epilepsy. J Physiol 591(4):807–822. https://doi.org/10.1113/jphysiol.2012.238154.

Carrillo-Reid L, Tecuapetla F, Tapia D, Hernández-Cruz A, Galarraga E, Drucker-Colin R, Bargas J (2008) Encoding network states by striatal cell assemblies. J Neurophysiol 99:1435–1450. https://doi.org/10.1152/jn.01131.2007.

Carrillo-Reid L, Tecuapetla F, Ibáñez-Sandoval O, Hernández-Cruz A, Galarraga E, Bargas J (2009) Activation of the cholinergic system endows compositional properties to striatal cell assemblies. J Neurophysiol 101:737–749. https://doi.org/10.1152/jn.90975.2008.

Carrillo-Reid L, Yang W, Bando Y, Peterka DS, Yuste R (2016) Imprinting and recalling cortical ensembles. Science 353 (6300):691–694. https://doi.org/10.1126/science.aaf7560.

Chen TS, Wardill TJ, Sun Y, Pulver SR, Renninger SL, Baohan A, Schreiter ER, Kerr RA, et al. (2013) Ultra-sensitive fluorescent proteins for imaging neuronal activity. Nature 499(7458):295–300. https://doi.org/10.1038/nature12354.

Chang M, Dian JA, Dufour S, Wang L, Chameh HM, Ramani M, Zhang L, Carlen PL, et al. (2018) Brief activation of GABAergic interneurons initiates the transition to ictal events through post-inhibitory rebound excitation. Neurobiol Dis 109:102–116. https://doi.org/10.1016/j.nbd.2017.10.007.

Churchland MM, Cunningham JP, Kaufman MT, Foster JD, Nuyujukian P, Ryu SI, Shenoy KV (2012) Neural population dynamics during reaching. Nature 487(7405):51–56. https://doi.org/10.1038/nature11129.

Cohen I, Huberfeld G, Miles R (2006) Emergence of disinhibition-induced synchrony in the CA3 region of the guinea pig hippocampus in vitro. J Physiol 570(Pt 3):583–594. https://doi.org/10.1113/jphysiol.2005.097899.

Colizza V, Flammini A, Serrano MA, Vespignani A (2006) Detecting rich-club ordering in complex networks. Nat Phys 2:110–115. https://doi.org/10.1038/nphys209.

Cossart R, Aronov D, Yuste R (2003) Attractor dynamics of network UP states in the neocortex. Nature 423:283–288. https://doi.org/10.1038/nature01614.

Cossart R (2014) Operational hub cells: a morpho-physiologically diverse class of GABAergic neurons united by a common function. Curr Opin Neurol 26:51–56. https://doi.org/10.1016/j.conb.2013.12.002.

de Curtis M, Jefferys JGR, Avoli M (2012) Interictal epileptiform discharges in partial epilepsy: complex neurobiological mechanisms based on experimental and clinical evidence. In: Noebels JL, Avoli M, Rogawski MA, editors. Jasper's basic mechanisms of the epilepsies. Bethesda (MD): National Center for Biotechnology Information (US). p. 303–325.

de la Prida LM, Huberfeld G, Cohen I, Miles R (2006) Threshold behavior in the initiation of hippocampal population bursts. Neuron 49(1):131–142. https://doi.org/10.1016/j.neuron.2005.10.034.

Dechery JB, MacLean JN (2017) Emergent cortical circuit dynamics contain dense, interwoven ensembles of spike sequences. J Neurophysiol 118:1914–1925. https://doi.org/10.1152/jn.00394.2017.

DeMarse TB, Pan L, Alagapan S, Brewer GJ, Wheeler BC (2016) Feed-forward propagation of temporal and rate information between cortical populations during coherent activation in engineered in vitro networks. Front Neural Circuits 10(32). https://doi.org/10.3389/fncir.2016.00032.

Derchansky M, Jahromi SS, Mamani M, Shin DS, Sik A, Carlen PL (2008) Transition to seizures in the isolated immature mouse hippocampus: a switch from dominant phasic inhibition to dominant phasic excitation. J Physiol 15586(2):477–494. https://doi.org/10.1113/jphysiol.2007.143065.

Feldt S, Bonifazi P, Cossart R (2011) Dissecting functional connectivity of neuronal microcircuits: experimental and theoretical insights. Trends Neurosci 34(5):225–236. https://doi.org/10.1016/j.tins.2011.02.007.

Fornito A, Zalesky A, Bullmore ET (2016) Fundamentals of brain network analysis. London: Academic Press.

Fries P (2005) A mechanism for cognitive dynamics: neuronal communication through neuronal coherence. Trends Cogn Sci 9:474–480. https://doi.org/10.1016/j.tics.2005.08.011.

Gonzalez-Sulser A, Wang J, Queenan BN, Avoli M, Vicini S, Dzakpasu R (2012) Hippocampal neuron firing and local field potentials in the in vitro 4-aminopyridine epilepsy model. J Neurophysiol 108:2568–2580. https://doi.org/10.1152/jn.00363.2012.

Grillner S, Markram H, De Schutter E, Silberberg G, LeBeau FE (2005) Microcircuits in action-from CPGs to neocortex. Trends Neurosci 28(10):525–533. https://doi.org/10.1016/j.tins.2005.08.003.

Gründemann J, Bitterman Y, Lu T, Krabbe S, Grewe BF, Schnitzer MJ, Lüthi A (2019) Amygdala ensembles encode behavioral states. Science 364:eaav8736. https://doi.org/10.1126/science.aav8736.

Harvey CD, Coen P, Tank DW (2012) Choice-specific sequences in parietal cortex during a virtual-navigation decision task. Nature 484(7392):62–68. https://doi.org/10.1038/nature10918.

Hebb DO (1949) The Organization of Behavior. J Clin Psychol 335.

Hippenmeyer S, Vrieseling E, Sigrist M, Portmann T, Laengle C, Ladle DR, Arber S (2005) A developmental switch in the response of DRG neurons to ETS transcription factor signalling. PLoS Biol 3:0878–0890.

Holmes GL, Lenck-Santini PP (2006) Role of interictal epileptiform abnormalities in cognitive impairment. Epilepsy Behav 8 (3):504–515. https://doi.org/10.1016/j.yebeh.2005.11.014.

Hongo Y, Takasu K, Ikegaya Y, Hasegawa M, Sakaguchi G, Ogawa K (2015) Heterogeneous effects of antiepileptic drugs in an in vitro epilepsy model – a functional multineuron calcium imaging study. Eur J Neurosci 42:1818–1829. https://doi.org/10.1111/ejn.12945.

Huberfeld G, de la Prida LM, Pallud J, Cohen I, Quyen MLV, Adam C, Clemenceau S, Baulac M, et al. (2011) Glutamatergic pre-ictal discharges emerge at the transition to seizure in human epilepsy. Nat Neurosci 14:627–635. https://doi.org/10.1038/nn.2790.

Humphries MK, Gurney K (2008) Network 'small-world-ness': A quantitative method for determining canonical network equivalence. PLoS ONE 3(4). https://doi.org/10.1371/journal.pone.0002051 e0002051.

Ibanez-Sandoval O, Hernández A, Floran B, Galarraga E, Tapia D, Valdiosera R, Erlij D, Aceves J, Bargas J (2006) Control of the subthalamic innervation of substantia nigra pars reticulata by D1 and D2 dopamine receptors. J Neurophysiol 95:1800–1811. https://doi.org/10.1152/jn.00620.2007.

Ikegaya Y, Aaron G, Cossart R, Aronov D, Lampl I, Ferster D, Yuste R (2004) Synfire chains and cortical songs: temporal modules of cortical activity. Science 304(5670):559–564. https://doi.org/10.1126/science.1093173.

Jirsa VK, Stacey WC, Quilichini PP, Ivanov AI, Bernard C (2014) On the nature of seizure dynamics. Brain 137:2210–2230. https://doi.org/10.1093/brain/awu133.

Karlócai MR, Kohus Z, Káli S, Ulbert I, Szabó G, Máté Z, Freund TF, Gulyas AI (2014) Physiological sharp wave-ripples and interictal events in vitro: what's the difference? Brain 137:463–485. https://doi.org/10.1093/brain/awt348.

Khoshkhoo S, Vogt D, Sohal VS (2017) Dynamic, cell-type-specific roles for GABAergic interneurons in a mouse model of optogenetically inducible seizures. Neuron 93:291–298. https://doi.org/10.1016/j.neuron.2016.11.043.

Krook-Magnuson E, Armstrong C, Oijala M, Soltesz I (2013) On-demand optogenetic control of spontaneous seizures in temporal lobe epilepsy. Nat Commun 4(1376). https://doi.org/10.1038/ncomms2376.

Lampl I, Reichova I, Ferster D (1999) Synchronous membrane potential fluctuations in neurons of the cat visual cortex. Neuron 22:361–374. https://doi.org/10.1016/S0896-6273(00)81096-X.

Lévesque M, Chen LY, Hamidi S, Avoli M (2018) Dynamic interneuron-principal cell interplay leads to a specific pattern of in vitro ictogenesis. Neurobiol Dis 115:92–100. https://doi.org/10.1016/j.nbd.2018.04.004.

Litvak L, Delgutte B, Eddington D (2003) Improved neural representation of vowels in electric stimulation using desynchronizing pulse trains. J Acoust Soc Am 114(4 Pt 1):2099–2111. https://doi.org/10.1121/1.1612494.

Luczak A, Barthó P, Marguet SL, Buzsáki G, Harris KD (2007) Sequential structure of neocortical spontaneous activity in vivo. Proc Natl Acad Sci U S A 104(1):347–352. https://doi.org/10.1073/pnas.0605643104.

Markram H, Toledo-Rodriguez M, Wang Y, Gupta A, Silberberg G, Wu C (2004) Interneurons of the neocortical inhibitory system. Nat Rev 5:793–807. https://doi.org/10.1038/nrn1519.

Markram H, Muller E, Ramaswamy S, Reimann MW, DeFelipe J, Hill SL, Segev I, Schurmann F, et al. (2015) Reconstruction and simulation of neocortical microcircuitry. Cell 163:456–492. https://doi.org/10.1016/j.cell.2015.09.029.

Mosbah A, Tramoni E, Guedj E, Aubert S, Daquin G, Ceccaldi M, Félician O, Bartolomei F (2014) Clinical, neuropsychological, and metabolic characteristics of transient epileptic amnesia syndrome. Epilepsia 55(5):699–706. https://doi.org/10.1111/epi.12565.

Muldoon SF, Soltesz I, Cossart R (2013) Spatially clustered neuronal assemblies comprise the microstructure of synchrony in chronically epileptic networks. PNAS 110(9):3567–3572. https://doi.org/10.1073/pnas.1216958110.

Muldoon SF, Villette V, Tressard T, Malvache A, Reichinnek S, Bartolomei F, Cossart R (2015) GABAergic inhibition shapes interictal dynamics in awake epileptic mice. Brain 138:2875–2890. https://doi.org/10.1093/brain/awv227.

Newman MEJ (2006) Modularity and community structure in networks. PNAS 103(23):8577–8582. https://doi.org/10.1073/pnas.0601602103.

Ngugi AK, Bottomley C, Kleinschmidt I, Sander JW, Newton CR (2010) Estimation of the burden of active and life-time epilepsy: a meta-analytic approach. Epilepsia 51:883–890. https://doi.org/10.1111/j.1528-1167.2009.02481.x.

Oh SW, Harris JA, Ng J, Winslow B, Cain N, Mihalas S, Wang Q, Lau C, et al. (2014) A mesoscale connectome of the mouse brain. Nature 508:207–214. https://doi.org/10.1038/nature13186.

Pastalkova E, Itskov V, Amarasingham A, Buzsáki G (2008) Internally generated cell assembly sequences in the rat hippocampus. Science 321(5894):1322–1327. https://doi.org/10.1126/science.1159775.

Pérez-Ortega J, Duhne M, Lara-González E, Plata V, Gasca D, Galarraga E, Hernández-Cruz A, Bargas J (2016) Pathophysiological signatures of functional connectomics in parkinsonian and dyskinetic striatal microcircuits. Neurobiol Dis 91:347–361. https://doi.org/10.1016/j.nbd.2016.02.023.

Peters AJ, Chen SX, Komiyama T (2014) Emergence of reproducible spatiotemporal activity during motor learning. Nature 510 (7504):263–267. https://doi.org/10.1038/nature13235.

Reyes AD (2003) Synchrony-dependent propagation of firing rate in iteratively constructed networks in vitro. Nat Neurosci 6:593–599. https://doi.org/10.1038/nn1056.

Sadovsky AJ, MacLean JN (2013) Scaling of topologically similar functional modules defines mouse primary auditory and somatosensory microcircuitry. J Neurosci 33(35):14048–14060. https://doi.org/10.1523/JNEUROSCI.1977-13.2013.

Sakata S, Harris KD (2009) Laminar structure of spontaneous and sensory-evoked population activity in auditory cortex. Neuron 64:404–418. https://doi.org/10.1016/j.neuron.2009.09.020.

Sanchez-Vives MV, McCormick DA (2000) Cellular and network mechanisms of rhythmic recurrent activity in neocortex. Nat Neurosci 3(10):1027–1034. https://doi.org/10.1038/79848.

Sasaki T, Matsuki N, Ikeyaga Y (2007) Metastability of active CA3 networks. J Neurosci 27(3):517–528. https://doi.org/10.1523/JNEUROSCI.4514-06.2007.

Serafini R, Dettloff S, Loeb JA (2016) Neocortical slices from adult chronic epileptic rats exhibit discharges of higher voltages and broader spread. Neuroscience 322:509–524. https://doi.org/10.1016/j.neuroscience.2016.02.026.

Sessolo M, Marcon I, Bovetti S, Losi G, Cammarota M, Ratto GM, Fellin T, Carmignoto G (2015) Parvalbumin-positive inhibitory interneurons oppose propagation but favor generation of focal epileptiform activity. J Neurosci 35(26):9544–9557. https://doi.org/10.1523/JNEUROSCI.5117-14.2015.

She Q, Chen G, Chan RHM (2016) Evaluating the small-world-ness of a sampled network: functional connectivity of entorhinal-hippocampal circuitry. Sci Rep 6(21468). https://doi.org/10.1038/srep21468.

Smith EH, Schevon CA (2016) Toward a mechanistic understanding of epileptic networks. Curr Neurol Neurosci Rep 16:97. https://doi.org/10.1007/s11910-016-0701-2.

Theis L, Berens P, Froudarakis E, Euler T, Tolias AS, Bethge M (2016) Benchmarking spike rate inference in population calcium imaging. Neuron 90:471–482. https://doi.org/10.1016/j.neuron.2016.04.014.

Tremblay R, Lee S, Rudy B (2016) GABAergic interneurons in the neocortex: from cellular properties to circuits. Neuron 91:260–292. https://doi.org/10.1016/j.neuron.2016.06.033.

van den Heuvel MP, Sporns O (2011) Rich-club organization of the human connectome. J Neurosci 31(44):15775–15786. https://doi.org/10.1523/JNEUROSCI.3539-11.2011.

Vogelstein JT, Packer AM, Machado TA, Sippy T, Babadi B, Yuste R, Paninski L (2010) Fast nonnegative deconvolution for spike train inference from population calcium imaging. J Neurophysiol 104:3691–3704. https://doi.org/10.1152/jn.01073.2009.

Watts DJ, Strogatz SH (1998) Collective dynamics of 'small-world' networks. Nature 393:440–442. https://doi.org/10.1038/30918.

Zaitsev AV (2017) The role of GABAergic interneurons in the cortex and hippocampus in the development of epilepsy. Neurosci Behav Physiol 47(8):913–922. https://doi.org/10.1007/s11055-017-0491-2.

Zhou JL, Shatskikh TN, Liu X, Holmes GL (2007) Impaired single cell firing and long-term potentiation parallels memory impairment following recurrent seizures. Eur J Neurosci 25(12):3667–3677. https://doi.org/10.1111/j.1460-9568.2007.05598.x.

APPENDIX A. SUPPLEMENTARY DATA

Supplementary data to this article can be found online at https://doi.org/10.1016/j.neuroscience.2020.08.025.

(Received 9 June 2020, Accepted 18 August 2020)
(Available online 27 August 2020)